The effects of biofilms on tumor progression in a 3D cancer-biofilm microfluidic model

Y. Deng[1], L. Yang[2], S. L. Chua[2,3,4]*, B. L. Khoo[1]*

[1] Department of Biomedical Engineering, City University of Hong Kong, Hong Kong, China

[2] Department of Applied Biology and Chemical Technology, The Hong Kong Polytechnic University, Hong Kong, China

[3] State Key Laboratory of Chemical Biology and Drug Discovery, Hong Kong, China

[4] Shenzhen Key Laboratory of Food Biological Safety Control, The Hong Kong Polytechnic University, Hong Kong, China

* Contact:

Song Lin Chua (song-lin.chua@polyu.edu.hk)

The Hong Kong Polytechnic University

Kowloon, Hong Kong, SAR 999077, China

Bee Luan Khoo (blkhoo@cityu.edu.hk)

City University of Hong Kong

83 Tat Chee Avenue, Kowloon, Hong Kong, China

Abstract

Components within the tumor microenvironment, such as intratumoral bacteria (IB; within tumors), affect tumor progression. However, current experimental models have not explored the effects of extratumoral bacteria (EB; outside tumors) on cancer progression. Here, we developed a microfluidic platform to analyze the influence of bacterial distribution on bladder cancer progression under defined conditions, using uropathogenic *Escherichia coli*. This was achieved by establishing coating (CT) and colonizing (CL) models to simulate the different invasion and colonization modes of IB and EB in tumor tissues. We demonstrated that both EB and IB induced closer cell-cell contacts within the tumor cluster, but cancer cell viability was reduced only in the presence of IB. Interestingly, cancer stem cell counts increased significantly in the presence of EB. These outcomes were due to the formation of extracellular DNA-based biofilms by EB. Triple therapy of DNase (anti-biofilm agent), ciprofloxacin (antibiotic), and doxorubicin (anti-cancer drug) could effectively eradicate biofilms and tumors simultaneously. Our preclinical proof-of-concept provides insights into how bacteria influence tumor progression and facilitate future research in anti-biofilm cancer management therapies.

Keywords: Drug screening; microfluidic tumor models; biofilms; antibacterial agents, combinatorial therapy

1. Introduction

There is increasing evidence that tumors contain intratumoral bacteria (IB) (Geller et al. 2017; Poore et al. 2020), and the composition of the human tumor microbiome has recently been extensively studied in many human tumors (Nejman et al. 2020). Bacterial infections are linked to cancer development, especially in the digestive system and urinary system, which can cause chronic inflammation or produce carcinogenic metabolites, thereby leading to cancer-promoting effects **(Supplementary Table 1)** (Balkwill and Mantovani 2001; Louis et al. 2014). For example, clinical evidence indicated that *Escherichia coli* and *Clostridium nucleatum* had the carcinogenic potential for colorectal cancer patients (Arthur et al. 2014), while *Helicobacter pylori* infection was highly correlated with the risk of gastric and pancreatic cancer (Raderer et al. 1998; Wroblewski et al. 2010).

On the contrary, recent studies have shown that systemic bacterial infections could also exacerbate the disease state of cancer patients, which suggested that extratumoral bacteria (EB) could also play a role in tumor progression (Dejea and Sears 2016; Garrett 2019; Li et al. 2017). In addition, most cancer patients with sepsis were infected with antibiotic-resistant Gram-negative bacteria (Safdar and Armstrong 2011). Due to bacteremia, acquired immune system abnormalities caused by neutropenia in cancer patients had severely complicated chemotherapy (Montassier et al. 2013; Perez et al. 2014). The average recovery rate of patients from bacteremia was only 51.3% (Trecarichi and Tumbarello 2014). Inappropriate antibiotic treatment will worsen the prognosis and survival rate of patients (Elkrief et al. 2019; Hopkins et al. 2020). This implied that anti-cancer drug resistance caused by secondary infections is an urgent problem during cancer treatment.

Recent clinical studies have shown that bacteria could form multicellular biofilms that cover or infiltrate the interstitial tumor space of patients with colorectal cancer (CRC) (Dejea et al. 2014; Drewes et al. 2017), leading to the up-regulation of pro-inflammatory cytokines (such as IL-6) (Dejea et al. 2014). Animal studies have also shown that transplanting biofilms from cancer patients and even healthy individuals could induce tumor formation (Tomkovich et al. 2019). Although many clinical studies have revealed the correlation between bacterial infections and tumor progression (El-Mosalamy et al. 2012; Schwabe and Jobin 2013), this raised the question of whether EB could form biofilms within the tumor microenvironment and influence tumor progression.

Many bacteria models, such as flow chamber biofilm assays and Calgary biofilm assays, cannot accurately recapitulate the 3D structure of biofilms found *in vivo* (Coraça‐Hubér et al. 2012; Harrison et al. 2010). Furthermore, an increasing amount of studies suggest the importance of

spatial heterogeneity in tumor progression (Athanasakis et al. 2018; Lee et al. 2019; Shimada et al. 2010). In addition to tumor complexity, it is crucial to develop a well-defined model that can compare the effects of EB and IB on tumor progression. Here, we developed a microfluidic Platform to analyze the effects of IB and EB (PIEB) on tumor progression under defined conditions, using uropathogenic *Escherichia coli* (UPEC) and bladder cancer cell clusters. We found that EB could form extracellular DNA (eDNA) - dependent biofilms, which led to closer cell-cell contacts within the cancer cell clusters. Conversely, exposing tumor cells to IB reduced cell viability, indicating that tumors responded differently to IB and EB. Besides, the presence of EB also significantly increased the proportion of cancer stem cells (CSCs). CSCs are tumorigenic cells often associated with metastasis and poor patient prognosis (Charafe-Jauffret et al. 2010). Our results corroborated with the clinical observations of patients with colorectal tumors, where biofilms 'protected' tumors in patients with colorectal cancer by enhancing resistance to anti-cancer drugs (Dejea et al. 2018; Dejea et al. 2014; Drewes et al. 2017). We further demonstrated that the triple therapy of DNase (anti-biofilm agent), ciprofloxacin (antibiotic commonly used to urinary tract infections (UTIs), and doxorubicin (anti-cancer drug) could improve the eradication of biofilm-tumor complexes.

Our work introduces a conceptual framework that reveals how the distribution of bacteria in tumor tissues affects cancer cell phenotypes and tumor progression. We envisage that the PIEB device will facilitate further research on the role of antibacterial agents in cancer management.

2. Material and methods

2.1. Fabrication of the PIEB device

The master mold of the tapered microwell layer and the gradient generator for the culture medium were made using diffuser back-side lithography procedures, as previously described (Khoo et al. 2019). The tapered microwell was 150 × 250 × 150 μm (length × width × depth), and each array contains 300 microwells. The depth of the microchannel was 6 mm. The mold was hard-baked at 150℃ for five minutes (Khoo et al. 2016). Polydimethylsiloxane (PDMS) molds were made via double-casting. PDMS was prepared using the Sylgard 184 Silicone Elastomer Kit (Dow Corning, USA) via a thorough mixing of the base resin and curing agent in a ratio of 10:1 (w/w). After plasma treatment, the replica PDMS mold was exposed to trichloro (1H,1H,2H,2H-perfluorooctyl) silane (Sigma-Aldrich, # 448931, Germany) within a vacuum desiccator for at least 6 h. Polylactic acid (PLA) molds were fabricated for the barrier layer and the gradient generator using 3D printing. The three layers were assembled with plasma treatment for 5 min (high RF level, 700 mmtor), followed by baking for 2 h at 70℃.

2.2. Cell culture

The human bladder carcinoma cell line UMUC-3 (CRL-1749, ATCC) were maintained in modified Minimum Essential Medium Alpha (MEM α; Gibco, # 12561049, USA) supplemented with 10% (v/v) fetal bovine serum (FBS; Gibco, # 10270106, USA) and 1% (v/v) penicillin-streptomycin (Gibco, # 15140122, USA) at 37℃ with 5% CO_2 in a humidified environment. Cells were cultured in sterile T25 or T75 flasks (Jet BIOFIL, China), with growth media replaced every 48 h. Cultures were passaged at 80% confluence.

2.3. Optimizing seeding concentration

UMUC-3 cells were diluted to a concentration of 4×10^5 cells mL^{-1} and seeded into microchannels to achieve final concentrations of 1.7×10^4, 2.1×10^4, 3.5×10^4, 6.0×10^4 cells per channel. After 24 h of incubation under optimal conditions, *in situ* analysis of the size and cell viability of clusters were performed using optical and fluorescence microscopy, respectively.

2.4. Culturing bacterial strain and heat-inactivated bacteria

The uropathogenic *E. coli* strain UTI89 was transformed with the plasmid expressing the DsRed fluorescent protein, as previously described (King et al. 2015). The bacterial culture was grown in Luria-Bertani (LB) broth (BD Difco, # 244620, USA) at 37 ℃ to allow bacterial growth. Bacteria concentrations will be approximately 10^9 cells mL^{-1} after 24 h.

For heat inactivation experiments, the bacterial suspension was heat-inactivated at 90℃ for 16 h. The suspension was plated onto LB agar for CFU counting to ensure that no colonies had grown, indicating that the bacteria were inactivated.

2.5. Establishment of coating (CT) and colonizing (CL) models

70 % (v/v) ethanol (EtOH; UNI-CHEM) was added to channels to sterilize the platform and remove air bubbles. 1× phosphate-buffered saline (PBS; Gibco, # 10010049, USA) was used to remove residual EtOH, and the microwell layer was then coated with 50 μL of 2.5 % bovine serum albumin (v/v) (BSA) (Sigma-Aldrich, # A9418-5G, Germany) to prevent cell adhesion to the channels. The capacity of each channel was 150 μL. UMUC-3 cell clusters in the microchannels could be stained *in situ* with Hoechst dye (Invitrogen, # H1399, USA) for 30 minutes to visualize cell nuclei or biofilm. Imaging and downstream analysis were carried out *in situ* after 1 h, 9 h, and 24 h of infection. UMUC-3 cell clusters without bacteria were used as negative controls.

For CT models, bacterial suspension was centrifuged for 10,000 rpm. LB supernatant was removed and replaced with antibiotic-free MEM α (10% supplemented with FBS) at the required multiplicity of infection (MOI) rates (500:1, 100:1, or 1:1). Control groups corresponding to 0 h time points were obtained before the introduction of bacteria. For CL models, bacteria and UMUC-3 cells were mixed at respective ratios of 500:1, 100:1, or 1:1 prior to seeding within channels.

2.6. Culture morphology *in situ* analysis

The clusters formed in the microwell array were imaged *in situ* with an optical microscope (Nikon, Eclipse Ci-L, Japan). Images were captured at the proximal, medial, and distal parts of each channel to ensure uniform outcomes. The image processing, cluster size analysis, and the density of fluorescence signals were carried out using the ImageJ software.

2.7 Confocal laser scanning microscope (CLSM)

Before seeding into the device, UTI89 transformed with Tn7-GFP plasmid was grown in LB broth with 50 μg/mL ampicillin (Sigma-Aldrich, Germany) at 37℃ for 24 h. UMUC-3 cells were incubated with by 1 μM Cell Tracker Deep Red (Invitrogen, #C34565, USA) serum-free culture media at 37℃ for 30 min. After infection, the device was directly placed on the glass slide and imaged *in situ* via Leica TCS SP8 MP confocal microscope (Germany).

2.8 Cell viability and immunostaining

Nuclear dye Hoechst (blue) and Calcein-AM (green) Invitrogen, # C3100MP, USA) were added to the channels at a final concentration of 20 μM. Clusters were imaged after 30 min incubation at 37 ℃. For immunostaining, cell clusters were first washed with 1× PBS gently and treated with 100 μg/mL gentamicin for 2 h to kill extracellular bacteria, followed by 30 min incubation with antibodies (CD44, PE-Cyanine5, # 15-0441-82; CD24, fluorescein, #11-0241-82, eBioscience, USA) at a final concentration of 0.4 μg/mL. Using ImageJ for analysis, only single cancer cells stained by Calcein-AM were enumerated by specifying the size (25-250 μm^2) and circularity (0.3-1.0), where the smaller bacteria were not included.

2.9 Crystal violet staining

Clusters were washed gently with 1× PBS, followed by staining with 0.1% crystal violet dye (Sigma-Aldrich, # HT90132, Germany) for 1 min. The stained biofilm was washed with 1× PBS to remove unstained crystal violet dye (Mok et al. 2020) and imaged via the optical microscope.

2.10 Colony-forming units (CFU) analysis

100 μg/mL of gentamicin was introduced for 2 h to kill extracellular bacteria after infection (Chua et al. 2014). The gentamicin was unable to enter eukaryotic cells to kill intracellular bacteria. Following gentamicin treatment, the cells in the channels were washed with 1× PBS to remove residual gentamicin and lysed with ddH_2O to release the intracellular bacteria. As previously described (Chan et al. 2021),

bacterial suspensions were collected and serially diluted for growth on an LB agar plate at 37 ℃ for 24 h. The CFU mL^{-1} were tabulated by the average number of colonies × dilution factor × volume.

2.11 DNase treatment

To disrupt the biofilm, 1× DNase (1 U/μL, Roche, # 4716728001, Switzerland) diluted with fresh penicillin-streptomycin-free culture medium was added to channels after 1 h infection, followed by incubation under optimal conditions. DNase was removed after 8 h for downstream analysis *in situ*. Clusters without DNase treatment served as a control.

2.12 Drug treatments of biofilms and cancer cell clusters

The UTI89 UPEC isolate was grown in 2 mL LB at 37 ℃ with 200 rpm shaking for 16 hrs. First, the OD600 values of UTI89 cultured overnight in LB broth (bacterial culture: LB = 1:1000) were obtained with a 96-well plate (SPL Life Sciences, South Korea). Ciprofloxacin (Cipro) was added at respective concentrations to the biofilms (0–0.1 μg/mL) (Sigma-Aldrich, # 17850-5G-F, Germany) in an 8-well chamber (Ibidi, Germany) to determine the minimal inhibitory concentration (MIC) values. The 8-well chamber plate was incubated overnight at 37 °C. For triple-drug combinatorial treatments, 150 μl of fresh LB culture was added with 0.0125ug/ml Cipro, 1× DNase to each well. After 8 h incubation, biofilms were disrupted by repeated pipetting, vortexing, and sonication in an ice-cold water bath (10 minutes) before serially diluted for plating on LB agar plates. The plates were incubated at 37 ℃ for bacterial colony growth and subsequent enumeration of colonies. CFU mL^{-1} was tabulated as average colony number X dilution factor X volume.

The dose-response curves of doxorubicin for cancer cells from the CT and CL models were fitted and drawn using the Origin 9 software with five-parameter equations to calculate the half-maximal inhibitory concentration (IC50) values. The IC50 value was defined as the drug concentration value that resulted in 50% viability of cells and determined by the concentration value (x-axis) corresponding to the value at 50% cell viability (y-axis), as indicated on the dosage-response curve (Khoo et al. 2019).

2.13 Statistical analysis

The results were expressed as means ± standard deviation. Data groups were compared using the one-way ANOVA and Student's *t*-test to evaluate associations between independent variables, and the *P* values were obtained. Three independent trials were conducted in triplicates for each experiment.

3. Results

3.1. Development of the microfluidic platform to analyze the effects of IB and EB on tumor progression

To study the effects of IB and EB on the progression of bladder tumors under defined conditions, we developed an integrated microfluidic PIEB device, which consisted of four components: (i) a bottom microwell layer for tumor-bacteria cluster formation, (ii) a middle barrier layer to retain fluids, (iii) a top layer to generate drug gradients and (iv) a top layer for bacteria distribution (**Figure 1A-B**). The device was designed to fit a 100-mm dish, filled with a thin film of sterile deionized water and stored in a humidified chamber to minimize the evaporation of long-term cultures (Berthier et al. 2008). Since UTI caused by UPEC infection is a contributing factor to the development of bladder cancer, and UPEC is similarly associated with bladder cancer (Chagneau et al. 2020; El Shobaky et al. 2015), we utilized bladder cancer cells (UMUC-3) and the UPEC strain (UTI89) in this proof-of-concept study. The cells were uniformly suspended in the growth medium and seeded into each microchannel. The resultant 3D structured biofilms formed in the PIEB microfluidic device were highly representative of biofilms *in vivo* than the traditional 2D models (**Figure 1C**) (Ning et al. 2019). After 24 h, cancer cells formed uniform clusters in the center of each microwell, which could be processed for downstream analysis (**Figure 1D**).

We evaluated various cancer cell seeding concentrations (corresponding to 17 - 60 cells per microwell) to determine the optimal cluster size for effective, compact, and viable cancer cell cluster establishment (**Supplementary Figure 1**). As determined by Calcein-AM dye labeling, a seeding concentration of 2.1×10^4 cells per channel resulted in the highest proportion of viable cells after 24 h. However, the cell viability of clusters seeded at a concentration of 3.5×10^4 cells per channel (77.07 ± 14.73%) was comparable to that of cultures seeded at a concentration of 2.1×10^4 cells per channel (77.49 ± 14.62%). We also evaluated the morphological parameters of cancer clusters, specifically cluster size. The cluster boundary was obtained by analyzing the gray value of phase-contrast images (**Supplementary Figure**

238 **2**). The seeding concentration of 3.5×10^4 cells per channel could produce clusters of a size range
239 (corresponding to ~ 35 cells per microwell; 8112.46 ± 921.99 μm^2) that were clinically comparable to
240 that of large cancer microclusters *in vivo* (~ 50 cells) (Cho et al. 2012; Molnar et al. 2001). Therefore,
241 the seeding concentration of 3.5×10^4 cells per channel was used in subsequent analyses.

242

243 **3.2. The distribution of bacteria in the tumor microenvironment affects the morphology and**
244 **viability of cancer cells**

245 To evaluate the pathological effects of bacterial distribution in the tumor microenvironment on the
246 growth and phenotype of bladder cancer cells, we proposed two infection models, the colonization model
247 (CL) and the coating model (CT), to reflect the difference in response for cancer cells in the presence of
248 IB and EB (**Figure 1E**). Specifically, IB in the CL model would be incorporated into tumor clusters,
249 while EB in the CT model would remain on the surface of the tumor clusters.

250 The CT and CL infection models were established and analyzed under various MOIs (bacteria: cancer
251 cell) and time points (1 h, 9 h, and 24 h) (**Figure 2A-D**). These time points were selected based on
252 previous UTI89 and SW480 co-culture studies, albeit the focus of these studies was on the pathogenic
253 effects of bacteria in murine models (Yu et al. 2017). Although higher MOIs (> 10:1) of bacteria were
254 often used to rapidly establish infections in animal and *in vitro* models (Billips et al. 2007; Dalmasso et
255 al. 2014; Santos et al. 2005), we chose a wider range of low to high MOIs (1:1, 100:1, and 500:1) to
256 mimic *in vivo* infection rates for higher clinical relevance (Anker et al. 2018).

257 Using Calcein-AM and Hoechst staining to observe the boundaries of cancer cell clusters, we found that
258 9 h after infection with a lower MOI (1:1 and 100:1), the size of the cancer cell clusters in CT and CL
259 models decreased (**Figure 2E-F**). Compared with the clusters from the CT model, the cluster size
260 decreased more significantly in the clusters derived from the CL model. For all infection time points
261 obtained by using the CL model in the case of lower MOI, the cluster size was significantly reduced after
262 9 h of infection (compared with 1 h of infection; MOI 1:1 – by 2.08 times; MOI 100:1 – by 2.09 times)
263 (**Figure 2E**). At lower MOIs, the size of the clusters obtained by the CL model within 1 h after infection
264 was comparable. However, higher MOI (500:1) with the CL model resulted in smaller clusters only
265 within 1 h after infection (**Figure 2E**). Interestingly, within 1 h after infection, at lower MOIs (1:1 and
266 100:1), the cluster size obtained with the CL model was still larger than the uninfected control cluster,
267 reflecting the infiltration and subsequent proliferation of IB within the cluster.

To evaluate the influence of the distribution of bacteria in the tumor microenvironment on the viability of cancer cells, clusters in the CT and CL models were labeled with Calcein-AM to reflect the proportion of viable cells (**Figure 2G-H**). We demonstrated that the presence of EB in the CT model did not lead to cancer cell killing, while the rapid and massive proliferation of colonized IB caused the reduction of cell viability, which was also previously observed to kill cancer cells through mechanisms involving growth inhibitors or hemolysin (Elliott et al. 2011; Smith et al. 2006). Specifically, even after 24 h of infection with all MOIs, the proportion of cluster cell viability in the CT model remained above 80% (**Figure 2G**). In the CL model at higher MOI (500:1), the presence of IB significantly reduced the viability of cancer cells within shorter infection periods (1 - 9 h). After 9 h of infection, the killing effect of cancer cells became more apparent under all MOIs, and the viability of cancer cells was significantly reduced as well in lower MOIs (**Figure 2H**). Since IB strains are commonly used as colonizing bacteria to treat cancer (Song et al. 2018; Zu and Wang 2014); therefore, our results indicated that the selection of bacteria for similar anti-cancer applications should be limited to bacteria with tumor-homing chemoreceptors.

With prolonged infection periods (48 h – 72 h), cancer cell lysis and reduction of cell viability was observed in CL models, but no significant changes in cluster size and cell viability were observed in CT models, albeit a slight reduction in cell viability was observed between 24 h and 48 h (**Supplementary figure 3**).

3.3. The effect on tumor progression and viability was attributed to the presence of biofilm formed by EB

Previous clinical studies have shown that biofilms could 'protect' colorectal tumors from anti-cancer drugs (Dejea et al. 2018; Dejea et al. 2014; Drewes et al. 2017). We aimed to demonstrate that the biofilms on tumor clusters were formed by EB. We visualized and quantified the biofilm biomass by crystal violet (CV) staining quantified the number of viable bacteria by CFU assays (Cegelski et al. 2009; Chua et al. 2014; Crémet et al. 2013; Ross et al. 2015). The presence of biofilm has been previously clinically shown to be the significant feature of proximal CRC (Drewes et al. 2017), which is also highly correlated with the risk and progression of CRC. As such, we aimed to utilize CV staining, a commonly used method for quantitative analysis of biofilms as the detection technique, to investigate the presence of biofilms. As shown by CV staining, in the CT model with EB, biofilm was formed on the periphery of the cancer cell clusters. In contrast, IB in the CL model entered the interstitial tumor space and cancer cells without forming a biofilm (**Figure 3A-B, Supplementary Figure 3A-B**). We further quantified the

CV staining via spectrometer analysis, by washing out biofilms stained with CV by 70% ethanol to 96-well plate and detecting the absorbance at a wavelength of 595 nm (Auger et al. 2006). The results indicated that though the OD595 values of solubilized CV from CT model were not higher than the ones from CL model due to the rapid proliferation of CL model under lower MOI (1:1 - 100:1) at earlier infecting period (1 h - 9 h), the biofilm mass formed in CT model after more than 9 h of infection was significantly more than the biofilm of CL model (**Figure 3C**).

The quantification of bacterial cell count further supported the presence of biofilm in the CT model. CFU counts were obtained after removing non-adherent bacteria. The CFU counts of adherent bacteria from the CT model were significantly higher than those from the CL model, especially at lower MOI 1:1 after 9 h of infection (by 2.25 times) (**Figure 3C, Supplementary Figure 3C-D**). Besides, since eDNA is a major component of UPEC biofilms (Devaraj et al. 2019; Devaraj et al. 2015), we hypothesized that eDNA was involved in biofilm formation in the CT model. This conclusion was also proved by the fluorescence intensity of UTI89-GFP under Z-stack imaging was used to quantify the amount of eDNA in the biofilm (**Figure 3E**). By measuring the intensity of UTI89-GFP fluorescence signal normalized to the background, we observed that the relative biofilm density on the periphery of cancer cell clusters of the CT model was higher than that of CL models, especially at higher MOI (500:1) (**Figure 3E, Supplementary figure 4F-G**). The 3D reconstructions of UMUC-3 labeled by Cell Tracker Deep Red and UTI89-GFP also clearly demonstrated the different bacteria colonizing situations in these two models and highlighted the presence of biofilm formation around the cancer cell clusters with the CT model. All these results corroborated our findings that EB formed eDNA-based biofilms were present only in the CT model.

3.4. Tumor metastatic potential was affected by the distribution of bacteria in the tumor microenvironment

Cancer stem-like properties are shown to be positively correlated with the cancer cell self-renewal and cancer metastasis (Chandrakesan et al. 2014). We demonstrated that the differential distribution of bacteria in CT and CL models affected the expression of CD44 and CD24, both of which are biomarkers corresponding to the CSC phenotype (**Figure 4A, Supplementary Figure 4**). CD24 is associated with the carcinogenicity of bladder cancer, and CD44 is positively correlated with the clinical stage of bladder cancer (Hofner et al. 2014). Specifically, under the CT model at all MOIs, the expression of CD44 in cancer cells increased significantly. Compared with clusters from the CL model, the proportion of $CD44^+$ cells in the CT model was significantly higher 9 h after infection, especially when the MOI was low (1:1)

(9 h: 1.23 times; **Figure 4B**). A lower degree of infection could have allowed cells to gradually adapt over time, inducing epithelial to mesenchymal transition, thereby increasing the proportion of CSCs (Massague and Obenauf 2016). At 9 h and 24 h after infection in the CT model, the proportion of $CD44^{+}CD24^{+}$ cells was also significantly higher than that in the CL model, especially in the case of low MOI (1:1) (9 h: 1.89 times; **Figure 4C-E**). When MOIs were higher at 100:1 and 500:1, the difference in the proportion of CSCs became less pronounced. The quantification of CD44 expression based on fluorescence intensity supported our findings that, compared with the CL model, the expression of CD44 in the CT model was significantly elevated 1-9 h after infection at all MOIs (**Figure 4F**). This implied that cancer cells within the clusters were driven towards a cancer stem-like phenotype. Therefore, in cancer patients with systemic infection during chemotherapy, EB could play an important role in tumor progression and metastasis.

3.5. Biofilm disrupting agents can eliminate pro-cancer effects generated by biofilms in the presence of bacterial infections

To test whether disrupting biofilms could impede tumor progression, the clusters were treated with DNase, a known anti-biofilm agent that can degrade eDNA and disrupt the biofilm matrix (Tetz et al. 2009a), at a clinically relevant concentration of 0.01 mg/mL (Tetz et al. 2009b). First, we quantified the CFU from the culture medium to confirm the efficacy of DNase for biofilm dispersal. The results obtained with both CT and CL models 9 h after infection at MOI 100:1 showed that CFU was increased only in the CT model after DNase treatment (**Figure 5A**).

After 9 h of infection with the CT model, treatment with DNase could reverse the effect of cluster size reduction (**Figure 6B**) but had no significant reduction in cluster size with the CL model (**Supplementary Figure 5A**). As DNase disrupted the biofilm formed by EB in the CT model, the viability of cancer cells was reduced, especially in higher MOI (100:1 and 500:1) compared with the untreated control group (**Figure 5C**). Compared with the untreated control, the expression intensity of CD44 and CD24 in the CT model was also reduced after DNase treatment. The reduction of CD44 and CD24 levels was most apparent after DNase treatment at higher MOIs (100:1 – 500:1), which could be due to the higher proportion of biofilm formed (**Figure 5D**). Therefore, DNase could effectively disrupt biofilms in the CT model.

3.6. Combinatorial treatment with the anti-cancer drug and antibacterial agents simultaneously eradicated biofilms and cancer cells within the CT model

Next, we asked whether the combinatorial treatment of DNase and antibiotics could effectively inhibit the growth of UTI89 biofilm. Anti-biofilm agent-antibiotic combinatorial treatment is crucial in disrupting biofilms to release embedded bacteria for antibiotic eradication (Yu and Chua 2020). Although UPEC biofilms are highly tolerant to commonly used antibiotics, Cipro was commonly used to treat UTI (Blango and Mulvey 2010; Mittal et al. 2015). Our evaluation indicated that the half-maximal inhibitory concentration (IC50) value of Cipro for UTI89 was 0.0125 μg/mL, and the minimal inhibitory concentration (MIC) value was 0.025 μg/mL (**Supplementary Figure 6A**. Specifically, the CFU from UTI89 biofilm under combinatorial treatment with 0.0125 μg/mL Cipro and DNase was significantly lower than that of untreated control and monotherapy groups (by 0.16 - 0.29 times) (**Supplementary Figure 6B**). These results underscored the benefits of using anti-biofilm agents and antibiotics in combinatorial treatment for cancer patients with systemic infections.

Furthermore, we proposed a triple therapy of DNase-Cipro-doxorubicin to eradicate resident biofilms and cancer clusters simultaneously (Figure 6A). As a control, we first confirmed that neither Cipro nor DNase had no adverse effect on the viability of non-infected cancer cells (**Figure 6B-C**). Then, we determined the IC50 value of doxorubicin on cancer cells with the CT and CL models (**Figure 6D**). We observed that the IC50 of doxorubicin on cancer cells with the CT model was significantly higher than that of cancer cells with the CL model (CT: 1.79 μM, CL: 1.59 μM). This indicated that the presence of biofilms produced in the presence of EB induced higher drug resistance. At MOI 1:1, the viability of cancer cells under the triple therapy of DNase (1×) – Cipro (0.025 μg/mL) - doxorubicin (IC50: 1.79 μM in CT model, 1.59 μM in CL model) was reduced after 72 h, as compared to monotherapy groups (**Figure 6E**). This implied that by the removal of biofilms, the drug resistance of cancer cells induced by inflammatory conditions such as systemic infection could be completely eradicated. Besides, the biofilms formed under both DOX only treatment and triple treatment for 72 h were tested via quantifying crystal-violet-stained biomass, where OD595 values of solubilized CV from CT and CL models were tested by a microplate reader under MOI 1:1. The results demonstrated that the degree of biofilm elimination under triple drug treatment was better than doxorubicin alone in both two models, which was better in CT models (CT models: DOX-only treatment, 2.029 ± 1.073, triple drug treatment, 1.551 ± 0.137; CL models, DOX-only treatment, 2.027 ± 0.220, triple drug treatment, 1.644 ± 0.097). This further confirmed that the triple drug strategy was to reduce the drug resistance of cancer cells by destroying the biofilm.

4. **Discussion**

Drug screening with clinically relevant models can facilitate the validation of new drug combinations prior to clinical trials (Wienkers and Heath 2005). Due to the complexity and dynamics of the tumor microenvironment, it is challenging to implement combinatorial treatments without rapid and cost-effective in vitro screening to reveal potential synergy or toxicity (Fearon and Vogelstein 1990; Hanahan and Weinberg 2011). Underlying issues such as the presence of inflammatory disease can further influence the effectiveness of treatment. Here, we described a proof-of-concept study using the microfluidic-based PIEB device to effectively study how bacteria influence the behavior of cancer cells in microclusters under well-defined conditions.

Bacteria strains can form the extratumoral biofilm, allowing them to colonize the surface of normal tissues and drive the development of colorectal cancer(Mirzaei et al. 2020). Since the EB biofilm is bacterial multicellular community held together by sticky extracellular exopolymeric substances, the biofilm matrix o protects biofilm bacteria from antibiotics and help host cells withstandanticancer chemotherapy(Dejea et al. 2018; Stewart and Costerton 2001). In this study, we proposed a novel triple combination therapy of an antibiofilm agent, an antibiotic and an anticancer drug to effectively eliminate both the biofilms and cancer cells.s. In rapidly infecting *in vitro* 2D models (1 – 2 h), UPEC strains can utilize type 1 and actin to invasive and efficiently multiply into bladder carcinoma cells and immortalized human urothelial cells to form the intracellular communities, which could further cause the distortion and exfoliation of host cells (Berry et al. 2009; Eto et al. 2006).

We demonstrated that EB could form biofilms on cancer cell clusters and induce cancer-promoting outcomes, which could be reversed by treatment with antibacterial agents. Our results provided potential insights for the combinatorial use of anti-cancer drugs and antibacterial agents in cancer patients with systemic bacterial infections.

We chose to use crystal violet stain, which was commonly used to stain biofilms in *in vitro* settings (Mok et al. 2020; O'Toole 2011), for the novel detection of biofilms in cancer cell clusters. To apply the biofilm as a potential marker in analysis of cancer with inflammation, we developed a spectrometer assay to detect biofilm biomass stained by crystal violet from different models, which could also be utilized for rapid detection and rapid treatment intervention.

Besides, clusters within the PIEB device were established within 24 h under optimal growth conditions, so those suitable therapeutic agents could be quickly screened and tested with a high throughput array.

The PIEB device was designed with a microwell array to generate uniform tumor clusters. The molds were produced using different strategies to suit the respective geometric geometry, dimensions, and tolerances in each layer. The deviation of shear rate and perfusion rate was negligible. The operation of the platform was straightforward and could be produced cost-effectively. The use of microfluidic technology enabled a robust performance with minimal requirements for cell and reagents, which opens more possibilities for applications involving rare primary cancer cells or clinical samples derived from patients. It has been previously reported that a microfluidic platform based on microwells could establish rare circulating tumor cell clusters from patient liquid (blood) biopsies, and the presence of cancer clusters reflected patient prognosis and survival rate (Khoo et al. 2019). We expect that further improvements to this assay can facilitate rapid, high-throughput, and inexpensive evaluation of drug response for drug discovery and provide insights into personalized patient treatment strategies.

5. Conclusions

Ourstudy demonstrated that the spatial distribution of bacteria in the tumor microenvironment could have different tumor progression outcomes. As demonstrated by the PIEB device, the biofilm formed in the CT model by EB could envelop tumor tissue, displaying higher tolerance to antibiotics (**Supplementary Figure 7A**) and inducing anti-cancer drug resistance (**Figure 6D-E**). In chronic infections such as pneumonia in patients with cystic fibrosis, similar protective effects due to the presence of biofilms have also been reported (De la Fuente-Núñez et al. 2013; Høiby et al. 2010). This could be attributed to the poor penetration of drugs through the dense biofilm matrix and the inactivation of anti-cancer drugs in the anaerobic/ acidic regions within the biofilms (Stewart and Costerton 2001). Although we demonstrated that the presence of biofilms formed by EB could lead to higher expression of CD44 and CD24 in the cancer cell clusters, the correlation between biofilm and cancer cell stemness remains unclear, which will warrant further mechanistic studies to verify their association. With the CL model, we demonstrated that IB could not form biofilms. Instead, IB adhered to cancer cells or infiltrated intratumoral spaces, corroborating with other reports (Elliott et al. 2011). These outcomes emphasized the importance of choosing appropriate treatment strategies to eliminate bacteremia in cancer patients during chemotherapy. The combinatorial use of anti-cancer drugs, anti-biofilm agents, and antimicrobials in clinical applications can help reduce the overall level of bacterial biofilm in the tumor microenvironment, thereby improving patient survival.

References

Anker, J.F., Naseem, A.F., Mok, H., Schaeffer, A.J., Abdulkadir, S.A., Thumbikat, P., 2018. Nature communications 9(1), 1-14.

Arthur, J.C., Gharaibeh, R.Z., Mühlbauer, M., Perez-Chanona, E., Uronis, J.M., McCafferty, J., Fodor, A.A., Jobin, C., 2014. Nature communications 5(1), 1-11.

Athanasakis, E., Xenaki, S., Venianaki, M., Chalkiadakis, G., Chrysos, E., 2018. Ann Gastroenterol 31(5), 525-534.

Auger, S., Krin, E., Aymerich, S., Gohar, M., 2006. Applied and environmental microbiology 72(1), 937-941.

Balkwill, F., Mantovani, A., 2001. The lancet 357(9255), 539-545.

Berry, R.E., Klumpp, D.J., Schaeffer, A.J., 2009. Infection and immunity 77(7), 2762-2772.

Berthier, E., Warrick, J., Yu, H., Beebe, D.J., 2008. Lab Chip 8(6), 860-864.

Billips, B.K., Forrestal, S.G., Rycyk, M.T., Johnson, J.R., Klumpp, D.J., Schaeffer, A.J., 2007. Infection and immunity 75(11), 5353-5360.

Blango, M.G., Mulvey, M.A., 2010. Antimicrobial agents and chemotherapy 54(5), 1855-1863.

Cegelski, L., Pinkner, J.S., Hammer, N.D., Cusumano, C.K., Hung, C.S., Chorell, E., Aberg, V., Walker, J.N., Seed, P.C., Almqvist, F., Chapman, M.R., Hultgren, S.J., 2009. Nat Chem Biol 5(12), 913-919.

Chagneau, C.V., Massip, C., Bossuet-Greif, N., Fremez, C., Motta, J.-P., Shima, A., Besson, C., Le Faouder, P., Cenac, N., Roth, M.-P., 2020. bioRxiv.

Chan, S.Y., Liu, S.Y., Seng, Z., Chua, S.L., 2021. The ISME Journal 15(1), 260-269.

Chandrakesan, á., Roy, B., Jakkula, L., Ahmed, I., Ramamoorthy, P., Tawfik, O., Papineni, R., Houchen, C., Anant, S., Umar, S., 2014. Oncogene 33(20), 2639-2654.

Charafe-Jauffret, E., Ginestier, C., Iovino, F., Tarpin, C., Diebel, M., Esterni, B., Houvenaeghel, G., Extra, J.-M., Bertucci, F., Jacquemier, J., 2010. Clinical cancer research 16(1), 45-55.

Cho, E.H., Wendel, M., Luttgen, M., Yoshioka, C., Marrinucci, D., Lazar, D., Schram, E., Nieva, J., Bazhenova, L., Morgan, A., Ko, A.H., Korn, W.M., Kolatkar, A., Bethel, K., Kuhn, P., 2012. Phys Biol 9(1), 016001.

Chua, S.L., Liu, Y., Yam, J.K., Chen, Y., Vejborg, R.M., Tan, B.G., Kjelleberg, S., Tolker-Nielsen, T., Givskov, M., Yang, L., 2014. Nature communications 5, 4462.

Coraça-Hubér, D.C., Fille, M., Hausdorfer, J., Pfaller, K., Nogler, M., 2012. Journal of Orthopaedic Research 30(7), 1176-1180.

Crémet, L., Corvec, S., Batard, E., Auger, M., Lopez, I., Pagniez, F., Dauvergne, S., Caroff, N., 2013. Diagnostic microbiology and infectious disease 75(3), 252-255.

Dalmasso, G., Cougnoux, A., Delmas, J., Darfeuille-Michaud, A., Bonnet, R., 2014. Gut microbes 5(5), 675-680.

Danese, S., Cremonini, F., Armuzzi, A., Candelli, M., Papa, A., Ojetti, V., Pastorelli, A., Di Caro, S., Zannoni, G., De Sole, P., 2001. Scandinavian journal of gastroenterology 36(3), 247-250.

De la Fuente-Núñez, C., Reffuveille, F., Fernández, L., Hancock, R.E., 2013. Current opinion in microbiology 16(5), 580-589.

Dejea, C.M., Fathi, P., Craig, J.M., Boleij, A., Taddese, R., Geis, A.L., Wu, X., Shields, C.E.D., Hechenbleikner, E.M., Huso, D.L., 2018. Science 359(6375), 592-597.

Dejea, C.M., Sears, C.L., 2016. Gut Microbes 7(1), 54-57.

Dejea, C.M., Wick, E.C., Hechenbleikner, E.M., White, J.R., Welch, J.L.M., Rossetti, B.J., Peterson, S.N., Snesrud, E.C., Borisy, G.G., Lazarev, M., 2014. Proceedings of the National Academy of Sciences 111(51), 18321-18326.

Devaraj, A., Buzzo, J.R., Mashburn-Warren, L., Gloag, E.S., Novotny, L.A., Stoodley, P., Bakaletz, L.O., Goodman, S.D., 2019. Proc Natl Acad Sci U S A 116(50), 25068-25077.
Devaraj, A., Justice, S.S., Bakaletz, L.O., Goodman, S.D., 2015. Mol Microbiol 96(6), 1119-1135.
Drewes, J.L., White, J.R., Dejea, C.M., Fathi, P., Iyadorai, T., Vadivelu, J., Roslani, A.C., Wick, E.C., Mongodin, E.F., Loke, M.F., 2017. NPJ biofilms and microbiomes 3(1), 1-12.
El-Mosalamy, H., Salman, T.M., Ashmawey, A.M., Osama, N., 2012. Infectious agents and cancer 7(1), 19.
El Shobaky, A., Abbas, M., Raouf, R., Zakaria, M.M., Ali-El-Dein, B., 2015. Egyptian Journal of Basic and Applied Sciences 2(3), 176-182.
Elkrief, A., El Raichani, L., Richard, C., Messaoudene, M., Belkaid, W., Malo, J., Belanger, K., Miller, W., Jamal, R., Letarte, N., 2019. Oncoimmunology 8(4), e1568812.
Elliott, N., Lee, T., You, L., Yuan, F., 2011. Integrative biology 3(6), 696-705.
Eto, D.S., Sundsbak, J.L., Mulvey, M.A., 2006. Cellular microbiology 8(4), 704-717.
Fearon, E.R., Vogelstein, B., 1990. Cell 61(5), 759-767.
Garrett, W.S., 2019. Science 364(6446), 1133-1135.
Geller, L.T., Barzily-Rokni, M., Danino, T., Jonas, O.H., Shental, N., Nejman, D., Gavert, N., Zwang, Y., Cooper, Z.A., Shee, K., Thaiss, C.A., Reuben, A., Livny, J., Avraham, R., Frederick, D.T., Ligorio, M., Chatman, K., Johnston, S.E., Mosher, C.M., Brandis, A., Fuks, G., Gurbatri, C., Gopalakrishnan, V., Kim, M., Hurd, M.W., Katz, M., Fleming, J., Maitra, A., Smith, D.A., Skalak, M., Bu, J., Michaud, M., Trauger, S.A., Barshack, I., Golan, T., Sandbank, J., Flaherty, K.T., Mandinova, A., Garrett, W.S., Thayer, S.P., Ferrone, C.R., Huttenhower, C., Bhatia, S.N., Gevers, D., Wargo, J.A., Golub, T.R., Straussman, R., 2017. Science 357(6356), 1156-1160.
Hanahan, D., Weinberg, R.A., 2011. Cell 144(5), 646-674.
Harrison, J.J., Stremick, C.A., Turner, R.J., Allan, N.D., Olson, M.E., Ceri, H., 2010. Nature protocols 5(7), 1236.
Hofner, T., Macher-Goeppinger, S., Klein, C., Schillert, A., Eisen, C., Wagner, S., Rigo-Watermeier, T., Baccelli, I., Vogel, V., Trumpp, A., 2014. Urologic Oncology: Seminars and Original Investigations, pp. 678-686. Elsevier.
Høiby, N., Bjarnsholt, T., Givskov, M., Molin, S., Ciofu, O., 2010. International journal of antimicrobial agents 35(4), 322-332.
Hopkins, A.M., Kichenadasse, G., Karapetis, C.S., Rowland, A., Sorich, M.J., 2020. European Urology.
Khoo, B.L., Grenci, G., Jing, T., Lim, Y.B., Lee, S.C., Thiery, J.P., Han, J., Lim, C.T., 2016. Sci Adv 2(7), e1600274.
Khoo, B.L., Grenci, G., Lim, J.S.Y., Lim, Y.P., Fong, J., Yeap, W.H., Bin Lim, S., Chua, S.L., Wong, S.C., Yap, Y.S., Lee, S.C., Lim, C.T., Han, J., 2019. Br J Cancer 120(4), 407-423.
King, J.E., Owaif, H.A.A., Jia, J., Roberts, I.S., 2015. Infection and immunity 83(7), 2605-2613.
Kostic, A.D., Chun, E., Robertson, L., Glickman, J.N., Gallini, C.A., Michaud, M., Clancy, T.E., Chung, D.C., Lochhead, P., Hold, G.L., 2013. Cell host & microbe 14(2), 207-215.
Lee, L.Y., De Paz, D., Lin, C.Y., Fan, K.H., Wang, H.M., Hsieh, C.H., Lee, L.A., Yen, T.C., Liao, C.T., Yeh, C.H., Kang, C.J., 2019. Cancer Med 8(14), 6185-6194.
Li, S., Konstantinov, S.R., Smits, R., Peppelenbosch, M.P., 2017. Trends in molecular medicine 23(1), 18-30.
Louis, P., Hold, G.L., Flint, H.J., 2014. Nature reviews microbiology 12(10), 661-672.
Massague, J., Obenauf, A.C., 2016. Nature 529(7586), 298-306.
Mirzaei, R., Mirzaei, H., Alikhani, M.Y., Sholeh, M., Arabestani, M.R., Saidijam, M., Karampoor, S., Ahmadyousefi, Y., Moghadam, M.S., Irajian, G.R., 2020. Microbial pathogenesis 142, 104052.
Mittal, S., Sharma, M., Chaudhary, U., 2015. Pathogens and global health 109(1), 26-29.
Mok, N., Chan, S.Y., Liu, S.Y., Chua, S.L., 2020. Food & Function.
Molnar, B., Ladanyi, A., Tanko, L., Sreter, L., Tulassay, Z., 2001. Clin Cancer Res 7(12), 4080-4085.

Montassier, E., Batard, E., Gastinne, T., Potel, G., de La Cochetière, M., 2013. European journal of clinical microbiology & infectious diseases 32(7), 841-850.
Nejman, D., Livyatan, I., Fuks, G., Gavert, N., Zwang, Y., Geller, L.T., Rotter-Maskowitz, A., Weiser, R., Mallel, G., Gigi, E., Meltser, A., Douglas, G.M., Kamer, I., Gopalakrishnan, V., Dadosh, T., Levin-Zaidman, S., Avnet, S., Atlan, T., Cooper, Z.A., Arora, R., Cogdill, A.P., Khan, M.A.W., Ologun, G., Bussi, Y., Weinberger, A., Lotan-Pompan, M., Golani, O., Perry, G., Rokah, M., Bahar-Shany, K., Rozeman, E.A., Blank, C.U., Ronai, A., Shaoul, R., Amit, A., Dorfman, T., Kremer, R., Cohen, Z.R., Harnof, S., Siegal, T., Yehuda-Shnaidman, E., Gal-Yam, E.N., Shapira, H., Baldini, N., Langille, M.G.I., Ben-Nun, A., Kaufman, B., Nissan, A., Golan, T., Dadiani, M., Levanon, K., Bar, J., Yust-Katz, S., Barshack, I., Peeper, D.S., Raz, D.J., Segal, E., Wargo, J.A., Sandbank, J., Shental, N., Straussman, R., 2020. Science 368(6494), 973-980.
Ning, E., Turnbull, G., Clarke, J., Picard, F., Riches, P., Vendrell, M., Graham, D., Wark, A.W., Faulds, K., Shu, W., 2019. Biofabrication 11(4), 045018.
O'Toole, G.A., 2011. J Vis Exp(47), 2437.
Perez, F., Adachi, J., Bonomo, R.A., 2014. Clinical infectious diseases 59(suppl_5), S335-S339.
Poore, G.D., Kopylova, E., Zhu, Q., Carpenter, C., Fraraccio, S., Wandro, S., Kosciolek, T., Janssen, S., Metcalf, J., Song, S.J., Kanbar, J., Miller-Montgomery, S., Heaton, R., McKay, R., Patel, S.P., Swafford, A.D., Knight, R., 2020. Nature 579(7800), 567-574.
Raderer, M., Wrba, F., Kornek, G., Maca, T., Koller, D.Y., Weinlaender, G., Hejna, M., Scheithauer, W., 1998. Oncology 55(1), 16-19.
Ross, B.N., Rojas-Lopez, M., Cieza, R.J., McWilliams, B.D., Torres, A.G., 2015. PloS one 10(10), e0141845.
Safdar, A., Armstrong, D., 2011. Clinical infectious diseases 53(8), 798-806.
Santos, S.A.d., Andrade, D.R.d., Andrade Júnior, D.R.d., 2005. Revista do Instituto de Medicina Tropical de São Paulo 47(2), 73-80.
Schwabe, R.F., Jobin, C., 2013. Nature Reviews Cancer 13(11), 800-812.
Shimada, Y., Ishii, G., Hishida, T., Yoshida, J., Nishimura, M., Nagai, K., 2010. J Thorac Oncol 5(7), 970-975.
Smith, Y.C., Grande, K.K., Rasmussen, S.B., O'Brien, A.D., 2006. Infection and immunity 74(1), 750-757.
Song, S., Vuai, M.S., Zhong, M., 2018. Infect Agent Cancer 13, 9.
Stewart, P.S., Costerton, J.W., 2001. The lancet 358(9276), 135-138.
Tetz, G.V., Artemenko, N.K., Tetz, V.V., 2009a. Antimicrob Agents Chemother 53(3), 1204-1209.
Tetz, G.V., Artemenko, N.K., Tetz, V.V., 2009b. Antimicrobial agents and chemotherapy 53(3), 1204-1209.
Tomkovich, S., Dejea, C.M., Winglee, K., Drewes, J.L., Chung, L., Housseau, F., Pope, J.L., Gauthier, J., Sun, X., Mühlbauer, M., 2019. The Journal of clinical investigation 129(4).
Trecarichi, E.M., Tumbarello, M., 2014. Current opinion in infectious diseases 27(2), 200-210.
Wienkers, L.C., Heath, T.G., 2005. Nat Rev Drug Discov 4(10), 825-833.
Wroblewski, L.E., Peek, R.M., Wilson, K.T., 2010. Clinical microbiology reviews 23(4), 713-739.
Xie, W., Huang, Y., Xie, W., Guo, A., Wu, W., 2010. PLoS One 5(5).
Yu, M., Chua, S.L., 2020. Medicinal Research Reviews 40(3), 1103-1116.
Yu, T., Guo, F., Yu, Y., Sun, T., Ma, D., Han, J., Qian, Y., Kryczek, I., Sun, D., Nagarsheth, N., Chen, Y., Chen, H., Hong, J., Zou, W., Fang, J.Y., 2017. Cell 170(3), 548-563 e516.
Zu, C., Wang, J., 2014. Crit Rev Microbiol 40(3), 225-235.

Acknowledgments

This study was supported by the City University of Hong Kong, which is funded by the Research Grants Council (RGC). This work was also supported by the Hong Kong Polytechnic University (BE2B), Environmental and Conservation Fund (ECF 49/2019), and State Key Laboratory for Chemical Biology and Drug Discovery.

Funding: City University of Hong Kong (9610430), which is funded by the Research Grants Council (RGC); Hong Kong Polytechnic University (BE2B); Environmental and Conservation Fund (ECF 49/2019) and State Key Laboratory for Chemical Biology and Drug Discovery.

Author contributions: Conceived and designed the experiments: BLK, SLC, YD. Performed the experiments: YD, LY. Analyzed the data: BLK, SLC, LY, YD. Contributed reagents/materials/analysis tools: BLK, SLC. Wrote the paper: BLK, SLC, LY, YD. All authors have read the manuscript.

Competing interests: One or more authors have a pending patent related to this work.

Data and materials availability: All data needed to evaluate the conclusions in the paper are present in the paper and/or the Supplementary Materials.

Figures and Tables

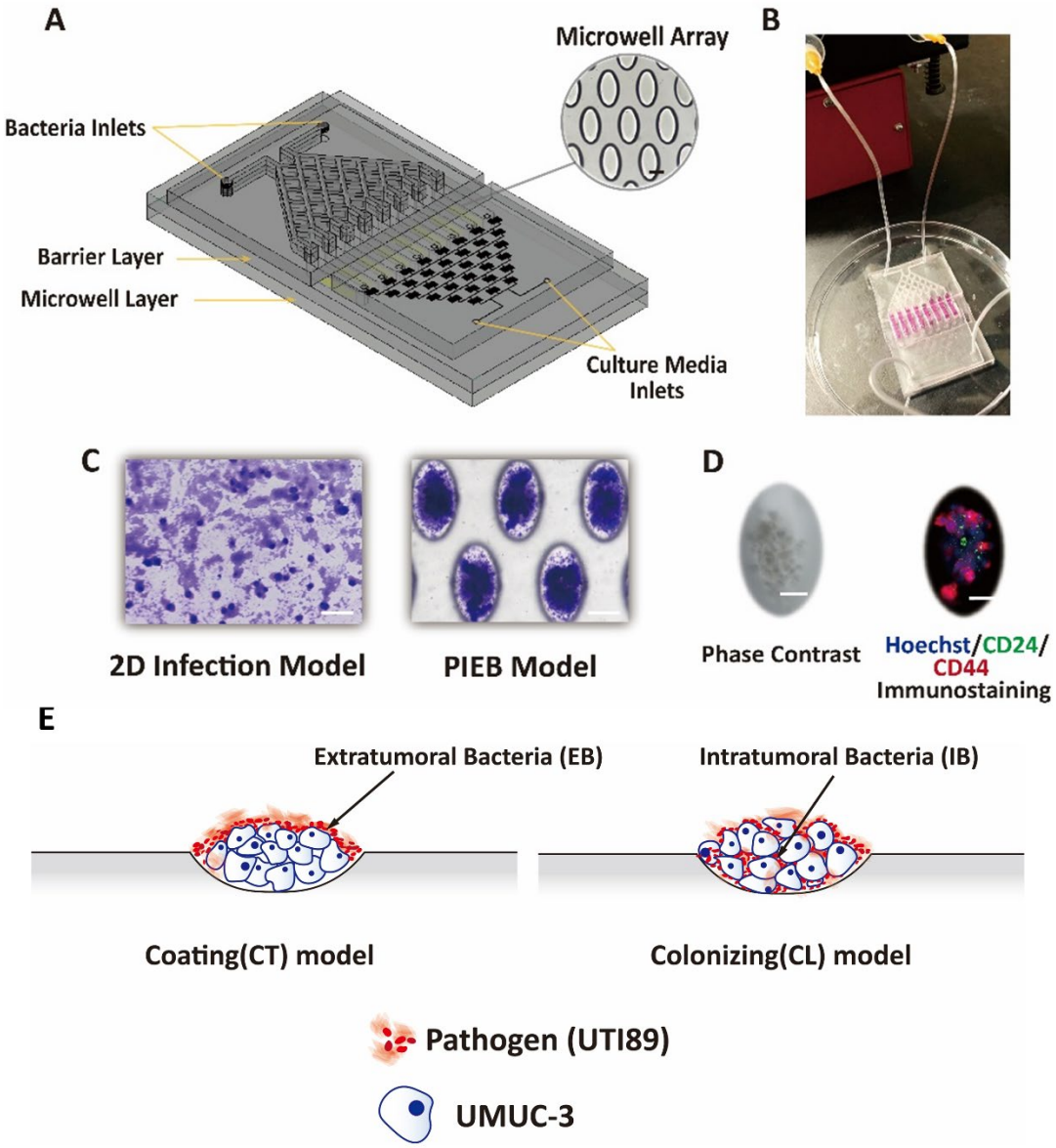

Figure 1. Development of a microfluidic PIEB device to analyze the roles of intratumoral and extratumoral Bacteria in cancer microbiome interactions. (A) Schematics of the microfluidic device. The microfluidic device consisted of three layers, with four inlets for bacteria and culture within the top layer. The barrier layer in the middle led to enclosed channels, while the bottom layer contained an array of tapered microwells for the formation of cell clusters. Scale bar, 100 μm. (B) Representative image of the device. Two inlets allowed parallel inflow of bacteria suspension and culture medium. (C) Comparison of *E. coli* biofilm formed in a 2D infection model (left) and the PIEB device (right). Scale bar, 100 μm. (D) Representative cell clusters in microwells under phase-contrast imaging (left) and

627 fluorescence imaging (right) after 24 h. The clusters were stained *in situ* with nuclear dye Hoechst (blue)
628 and CD24 (green), and CD44 (red) antibodies that targeted cancer stem cells. Scale bar, 50 μm. (E)
629 Cancer cell clusters from bacteria colonizing (CL) model and coating (CT) model were obtained under
630 well-defined conditions with moderations of operating procedures with the microfluidic PIEB device.

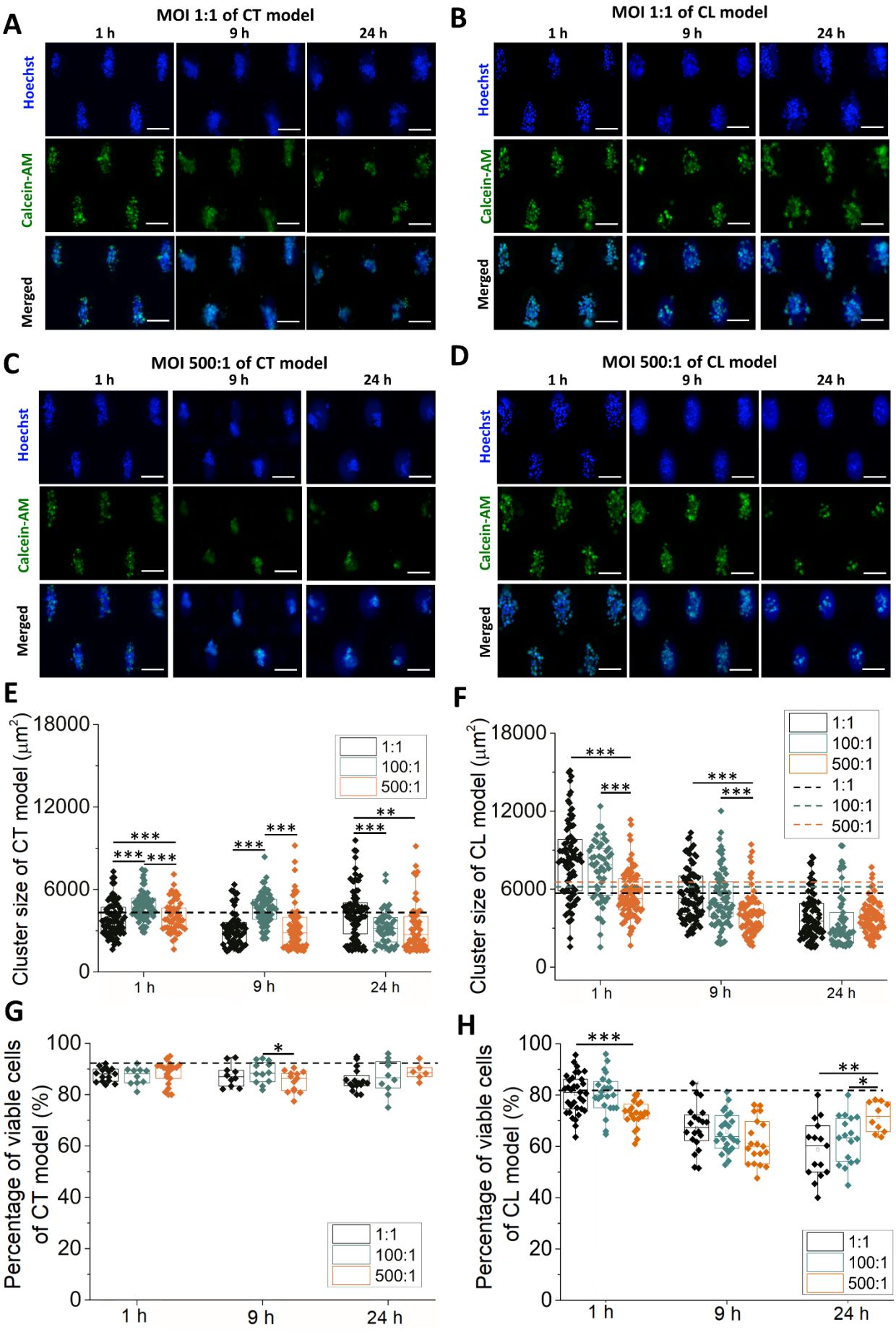
A
MOI 1:1 of CT model
1 h
9 h
24 h
Hoechst
Calcein-AM
Merged
B
MOI 1:1 of CL model
C
MOI 500:1 of CT model
D
MOI 500:1 of CL model
E
Cluster size of CT model (μm²)
18000
12000
6000
0
1:1
100:1
500:1
***
**
F
Cluster size of CL model (μm²)
G
Percentage of viable cells of CT model (%)
100
80
60
40
20
0
*
H
Percentage of viable cells of CL model (%)

631

Figure 2. The changes of morphology and viability of cancer cell clusters in the presence of bacterial inflammation. Representative images of clusters stained with Calcein-AM (green; live cells) and Hoechst (blue; nuclei) for the CL models and CT models after infection at 1 h (A-B) and 24 h (C-D) , respectively. Scale bar, 100μm. (C) Box plot of cluster size from the CT model after 24 h of infection under MOIs 500:1, 100:1, and 1:1. The average cluster size obtained before infection (4319.10 ± 2024.48 μm^2) was indicated by the dotted line. No significant differences in cluster size in the CT model as compared to non-infected clusters were observed. (D) Box plot of cluster size from the CL model after 24 h of infection under MOIs 500:1, 100:1, and 1:1. For all infection time points under the lower MOIs, the cluster size in the CL model was significantly reduced by more than two times (MOI 1:1 - 8178.95 ± 2963.23 μm^2 to 3923.60 ± 1760.40 μm^2; MOI 100:1 - 7418.05 ± 2329.95 μm^2 to 3548.64 ± 2156.04 μm^2). The average cluster sizes obtained by coculture of UMUC-3 and heat-killed UTI89 were indicated by dotted lines (MOI 1:1, 5842.08 ± 1896.00 μm^2; MOI 100:1, 6070.62 ± 1742.10 μm^2; MOI 500:1, 6181.752 ± 1209.80 μm^2). (G) Box plot of cell viability with the CT model after 24 h of infection under the MOIs of 500:1, 100:1, and 1:1. The average viability of the uninfected control group corresponding to the CT model was indicated by the dotted line (92.10 ± 5.07%). No significant differences in cancer cell viability in the CT model as compared to non-infected clusters were observed (MOI 1:1 - 88.56 ± 4.61%, MOI 100:1 – 80.16 ± 18.94%, MOI 500:1 – 88.89 ± 3.23). (H) Box plot of cell viability with the CL model after 24 h of infection under the MOIs of 500:1, 100:1, and 1:1. The viability of cancer cells was significantly reduced after at least 9 h of infection and was most apparent at later time points (MOI 1:1 - 80.04 ± 7.67% at 1 h to 58.76 ± 11.29% at 24 h; MOI 100:1 - from 80.50 ± 7.79% at 1 h to 62.68 ± 9.41% at 24 h). The average viability of the uninfected control group corresponding to the CL model was indicated by the dotted line (84.69 ± 5.61%). *** states for p values of < 0.001; ** states for p values of < 0.01, * states for p values < 0.05.

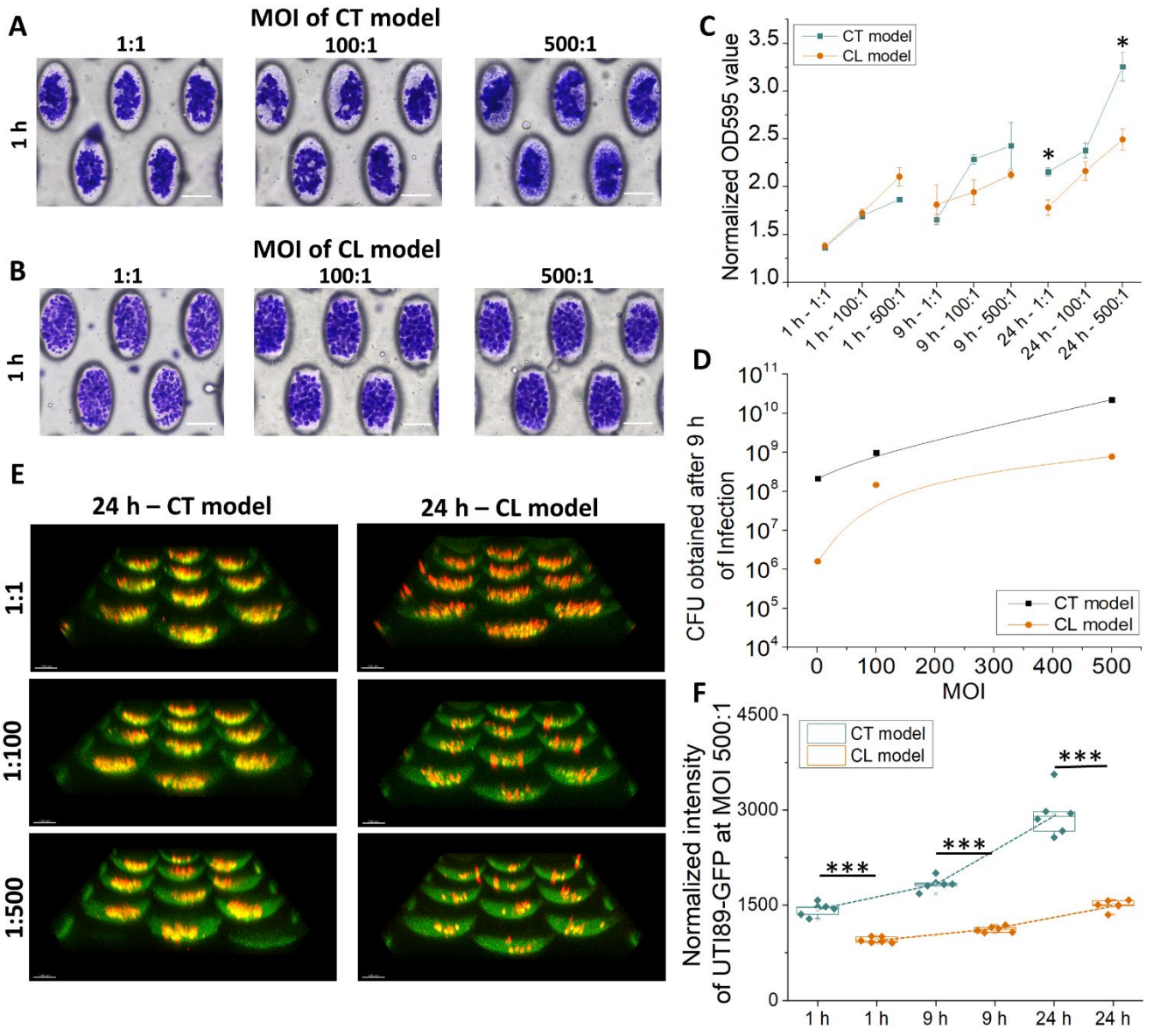

Figure 3. Biofilm was formed in the presence of extratumoral bacteria (EB) but not intratumoral bacteria (IB). Representative images of crystal violet staining to illustrate the presence of dense biofilm obtained with EB in the (A) CT model, but not IB in the (B) CL model 1 h after infection. Scale bar, 100 µm. (C) OD595 value of solubilized CV from CT and CL models after 24 h of infection under MOIs 500:1, 100:1, and 1:1 normalized to uninfected control group quantified the biofilms formed in different colonization states. (D) CFU was obtained at 9 h after infection to estimate the amount of biofilm formed with the CT and CL models. (E) 3D combinations of UTI89-GFP (green) formed in CT and CL models 24 h after infection, which indicated the exist of biofilm coating the UMUC-3 clusters in CT models. Scale bar, 100 µm. (F) Box plot demonstrating the intensity of UTI89-GFP normalized to background signals at MOI 500:1 from CT and CL models 24 h after infection. *** states for p values< 0.001.

667

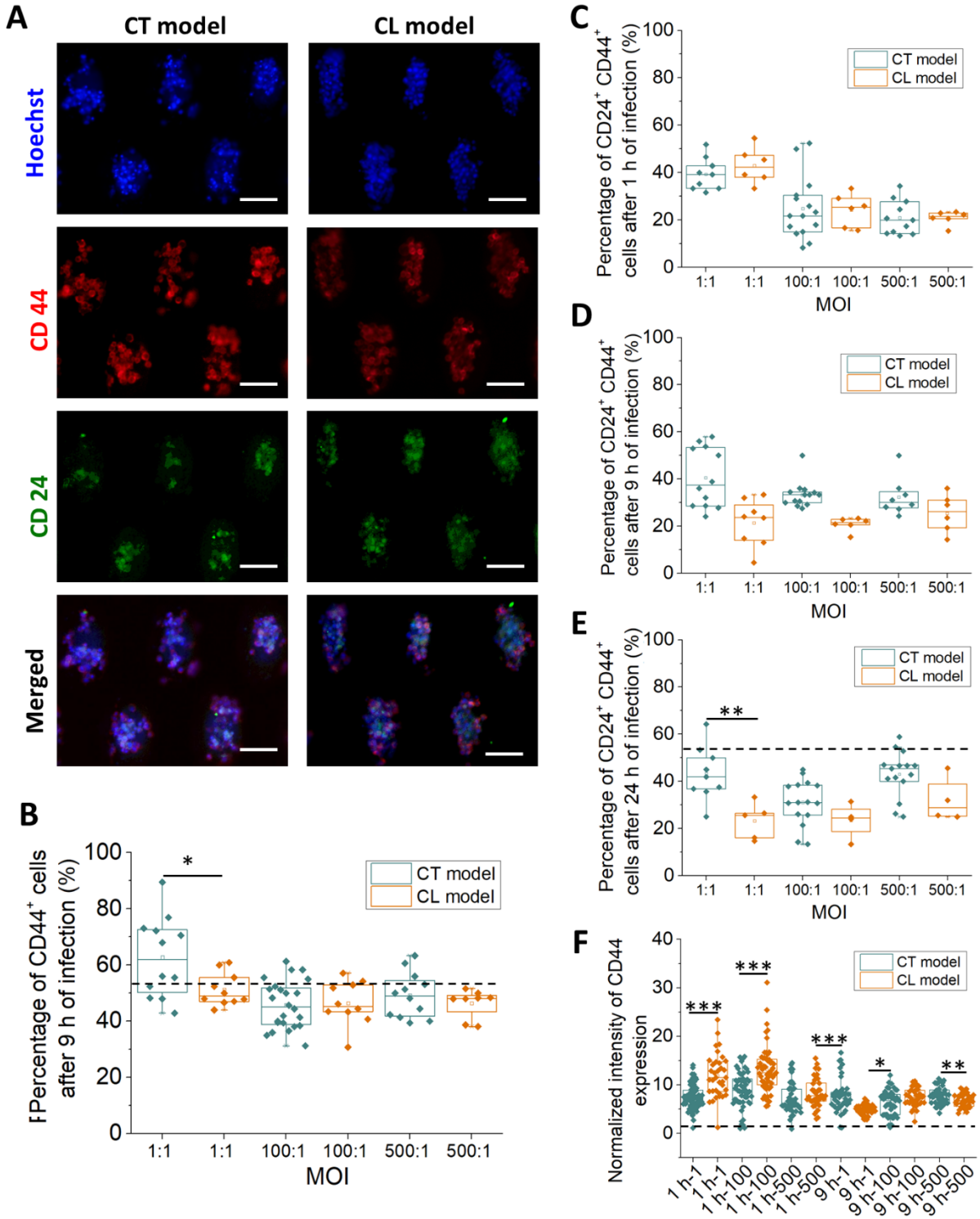

668

669 **Figure 4. The presence of biofilm increased the expression levels of biomarkers associated with the**
670 **cancer stem cell (CSC) phenotype.** (A) Representative images of clusters stained with Hoechst (blue),
671 CD24 (green), and CD44 (red) from the CL model (top) and CT model (bottom), respectively. (B)
672 Intensities of CD44 protein expression in cancer cells from the CT model and CL model after 1 h and 9

673 h of infection, respectively. Intensity values were normalized to that of the background. The intensity of
674 CD44 expression from uninfected control (28.94 ± 7.73 %) was indicated by the dotted line. (D) The
675 proportion of $CD24^+$ $CD44^+$ cancer cells in the clusters established under CT and CL models 9 h after
676 infection. (E) The proportion of $CD24^+$ $CD44^+$ cancer cells in the clusters established from the CT and
677 CL models after 24 h of infection. The proportion of $CD24^+CD44^+$ cells in the uninfected control group
678 (28.94 ± 7.73%) was indicated by the dotted line. (F) Intensities of CD44 expression in cancer cells from
679 the CT model and CL model after 1 h and 9 h of infection, respectively. Intensity values were normalized
680 to that of the background. The intensity of CD44 expression of uninfected control (53.07 ± 10.47 %)
681 was indicated by the dotted line. (F) The proportion of $CD44^+$ cancer cells in the CT and CL models after
682 9 h of infection. The proportion of $CD44^+$ cells in the uninfected control group (53.07 ± 10.47%) was
683 indicated by the dotted line. (C) The proportion of $CD24^+$ $CD44^+$ cancer cells in the clusters established
684 under CT and CL models after 1 h of infection. *** states for p values of < 0.001; ** states for p values
685 of < 0.01, * states for p values of < 0.05.

686

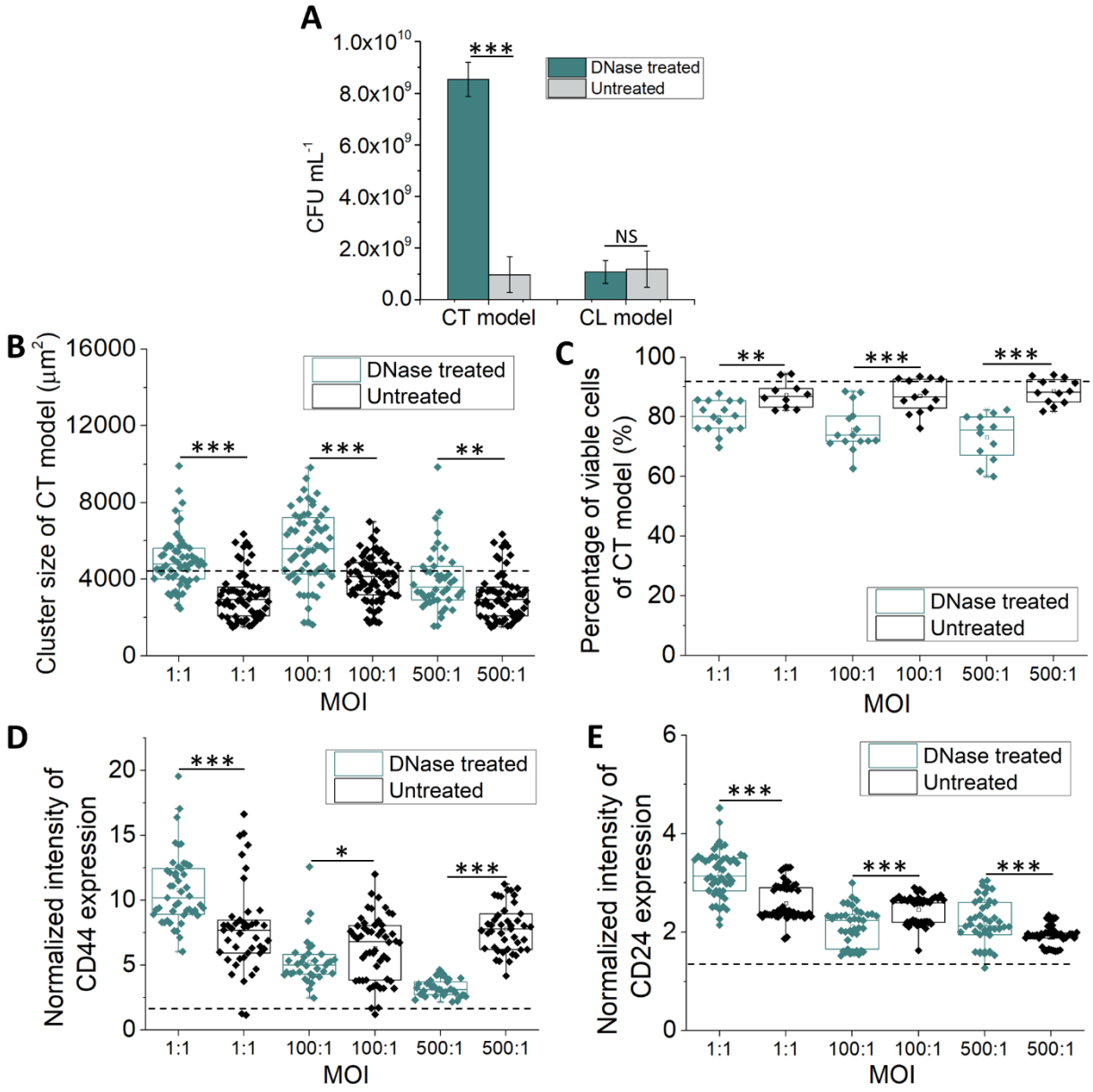

687

688 **Figure 5. DNase-induced biofilm disruption restores the phenotype induced by the presence of**
689 **biofilm.** (A) CFU counts from DNase treated and untreated culture medium with CT and CL models at
690 MOI 100:1. Models were established for 9 h prior to DNase treatment. CFU counts were significantly
691 decreased after DNase treatment in the CT model, confirming the presence of biofilms established only
692 in CT models with EB. (B) Cluster size in CT models after DNase treatment to disrupt the biofilm. The
693 average cluster size of uninfected cancer cell clusters was as indicated by the dotted line (4319.10 ±
694 2024.48 μm^2). (C) Cancer cell viability in CT models after DNase treatment to disrupt the biofilm. The
695 average viability of uninfected cancer cell clusters was as indicated by the dotted line (92.10 ± 5.07%).
696 (D) Normalized intensity of CD44 expression with cancer cells from the CT model, before and after

697 treatment with DNase. Models were established for 9 h prior to DNase treatment. The average CD44
698 intensity of the uninfected group was indicated by the dotted line (1.50 ± 0.33). Data was normalized to
699 background values. (F) Normalized intensity of CD24 expression with cancer cells from the CT model,
700 before and after treatment with DNase. Models were established for 9 h prior to DNase treatment. The
701 average CD24 intensity of the uninfected group was indicated by the dotted line (1.29 ± 0.22). Data was
702 normalized to background values. *** states for $p < 0.001$; ** states for $p < 0.01$.

703

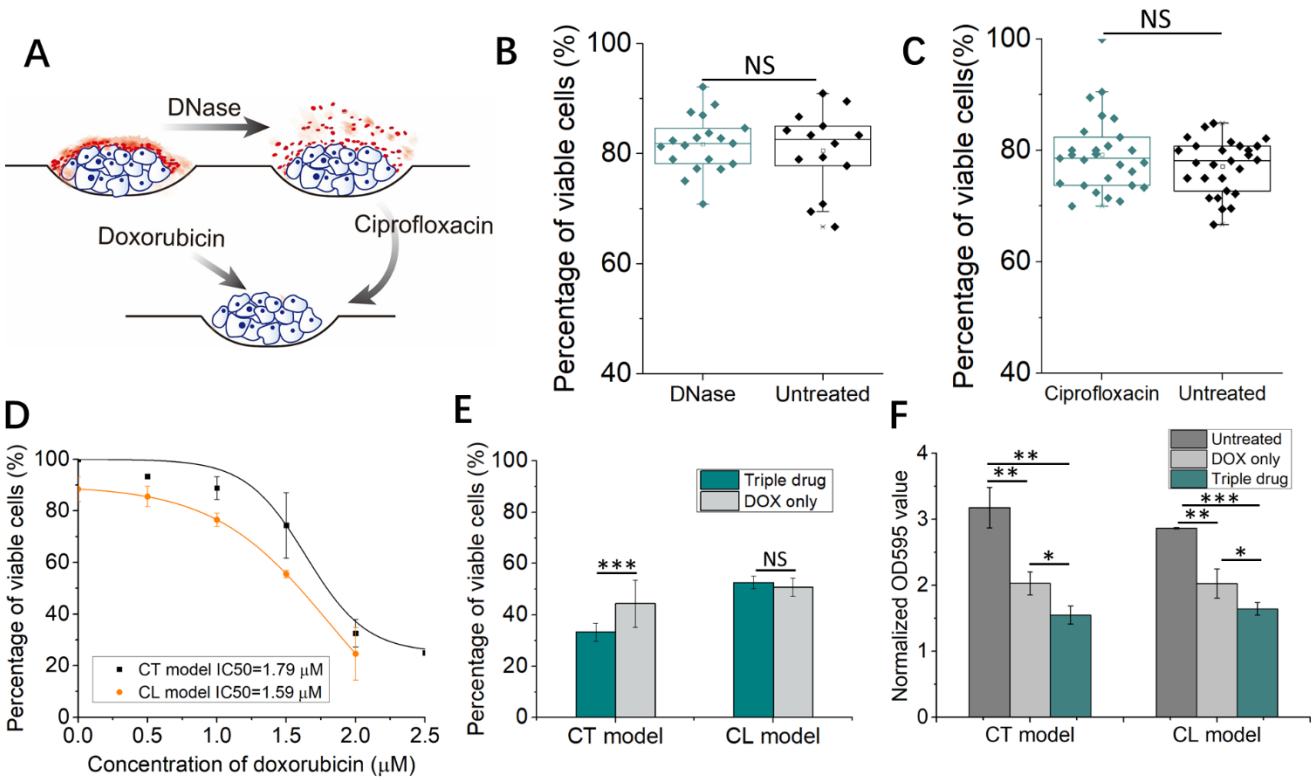

Figure 6. The triple-drug combinational treatment effectively eradicated anti-cancer drug resistance induced by the presence of bacterial biofilms. (A) Schematics demonstrating the combined efficacy of the triple-drug combinatorial treatment. DNase was used as the anti-biofilm agent, Cipro as the antibacterial agent, and doxorubicin as the anti-cancer drug to completely eradicate biofilms. (B) The viability of cancer cells in the uninfected control group before and after DNase treatment. (C) The viability of cancer cells before and after Cipro treatment for 24 h (MIC value: 0.025 μg/mL). NS = not significant. (D) Dose-response curves of doxorubicin for cancer cells with the CT model and the CL model at MOI 1:1. The IC50 values of doxorubicin for the CT model and the CL model were 1.79 μM and 1.59 μM, respectively. (E) The viability of cancer cells after triple-drug combinational treatment at MOI 1:1 for 72 h (Cipro (0.025 μg/mL), 1× DNase, and doxorubicin (at IC50 values) with the CT model and CL models, respectively. IC50 values of doxorubicin on cancer cells from the CT and CL models were 1.79 μM and 1.59 μM, respectively. (F) The OD595 value of solubilized CV from CT and CL models after DOX (at IC50 values) treatment and triple-drug treatment at MOI 1:1 for 72 h (Cipro (0.025 μg/mL), 1× DNase, and doxorubicin (at IC50 values). The untreated groups infected with UTI89 at MOI 1:1 for 72 h in both models were set as controls. *** states for p values of < 0.001; ** states for p values of < 0.01, * states for p values of < 0.05; NS = not significant.

Supplementary Materials

Supplementary Figures

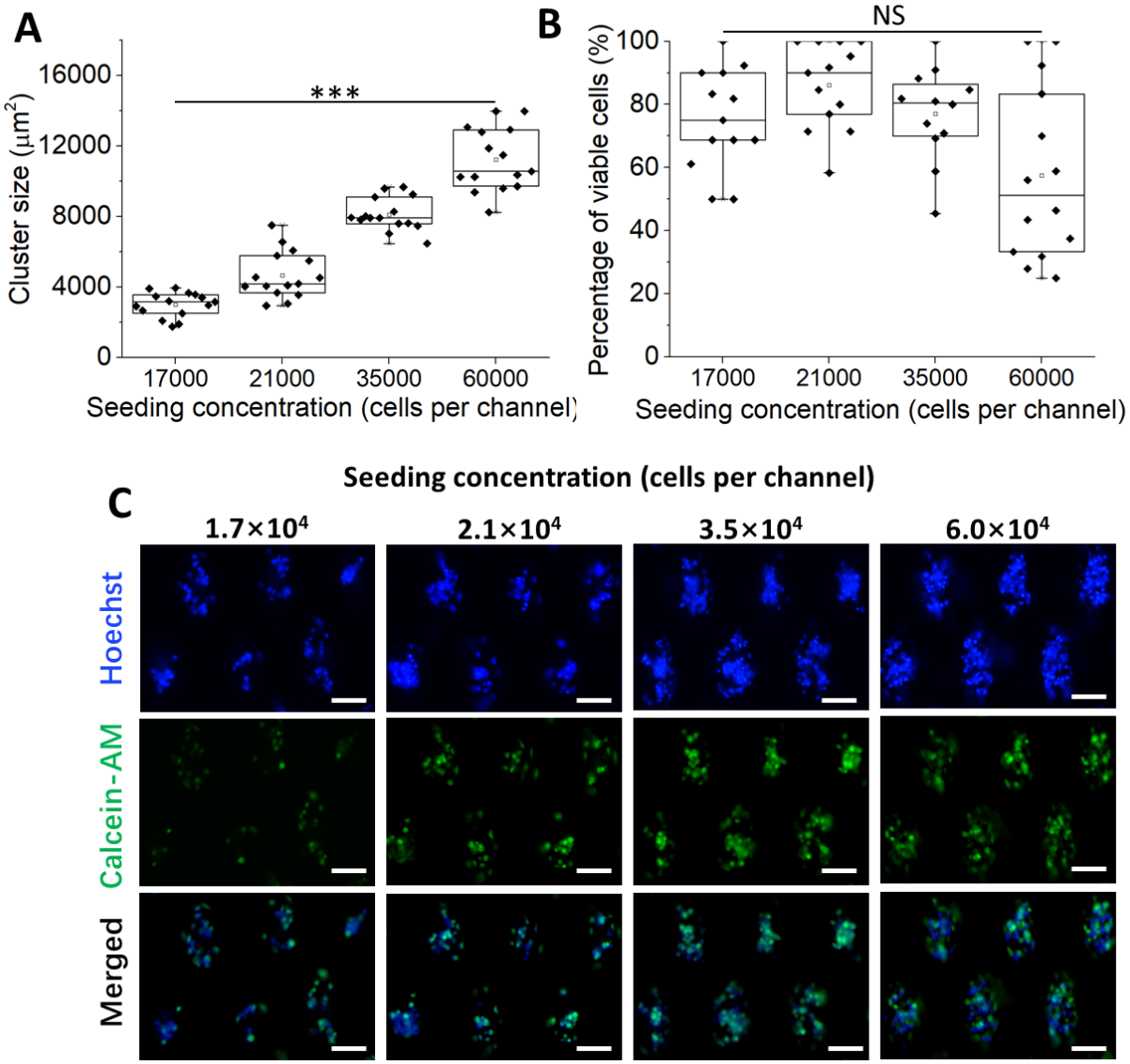

Supplementary figure 1. Optimization of seeding concentration. (A) Cluster size under various cell seeding concentrations. (B) Cell viability under various cell seeding concentration. The viability of cancer cells under all concentrations was high, above 75%. *** states for p values of < 0.001; NS = not significant. (C) Representative images of clusters stained with Calcein-AM (green) and Hoechst (blue) at various cell seeding concentrations. Scale bar, 100 μm.

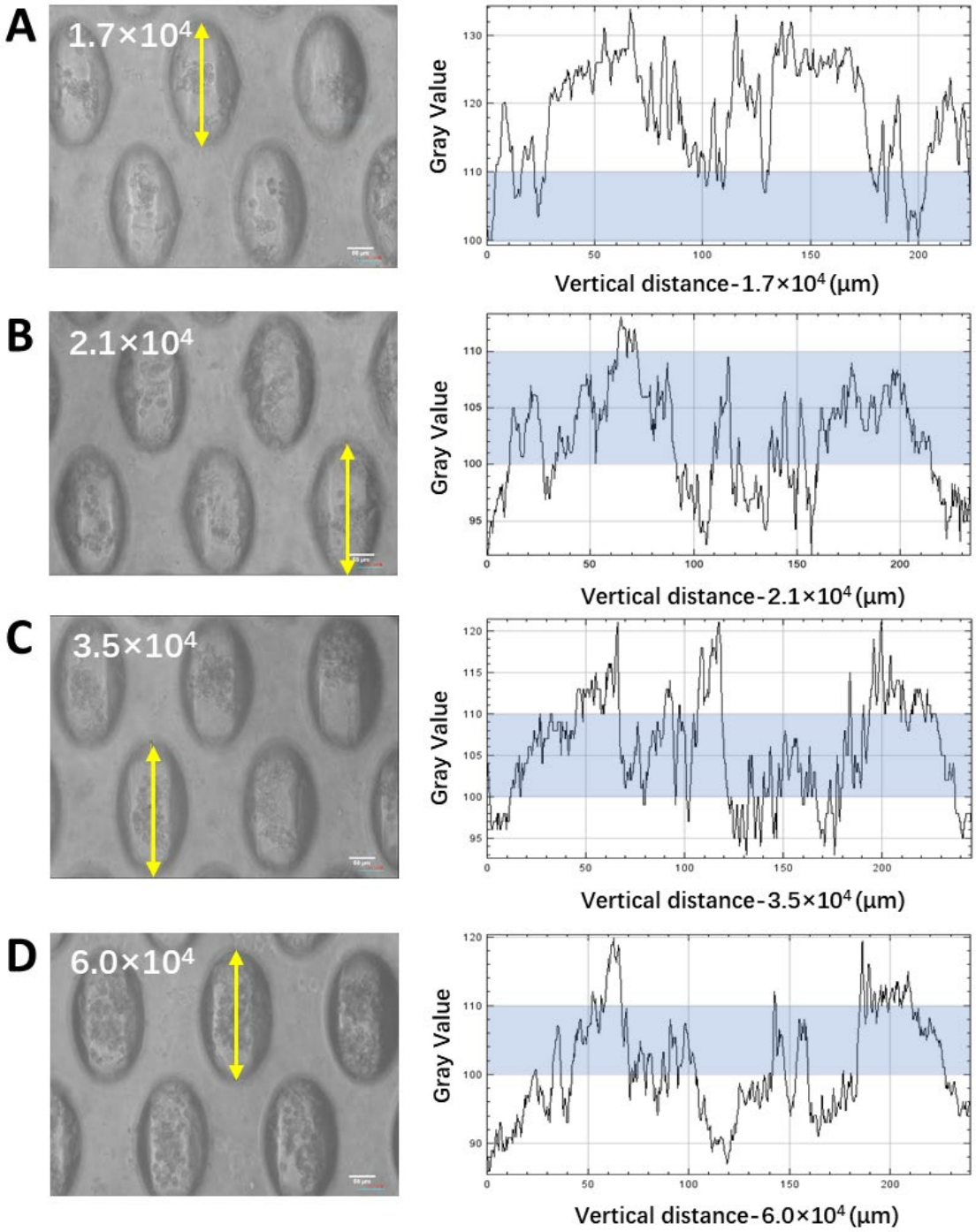

Supplementary figure 2. The gray values of representative clusters formed under different seeding concentration. (A) 1.7×10^4 cells per channel. (B) 2.1×10^4 cells per channel. (C) 3.5×10^4 cells per channel. (D) 6.0×10^4 cells per channel. Scale bar, 50 μm.

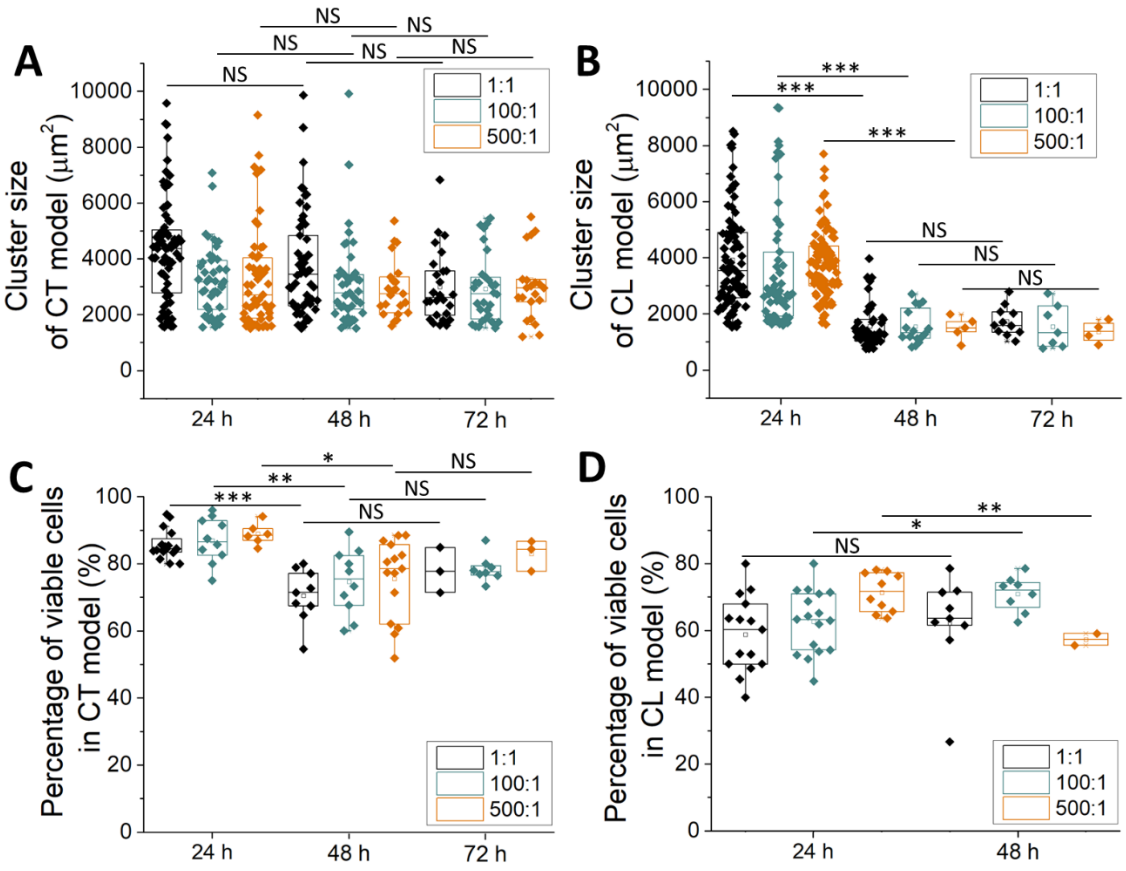

Supplementary figure 3. Trends of cluster morphology and cell viability after more than 24 h of infection. Cluster size per microwell under various MOIs in CT model (A) and CL model (B) at 48 h and 72 h after infection. Cell viability under various MOIs in CT model (C) and CL model (C) at 48 h and 72 h after infection. *** states for p values of < 0.001; ** states for p < 0.01; * states for p < 0.05; NS = not significant.

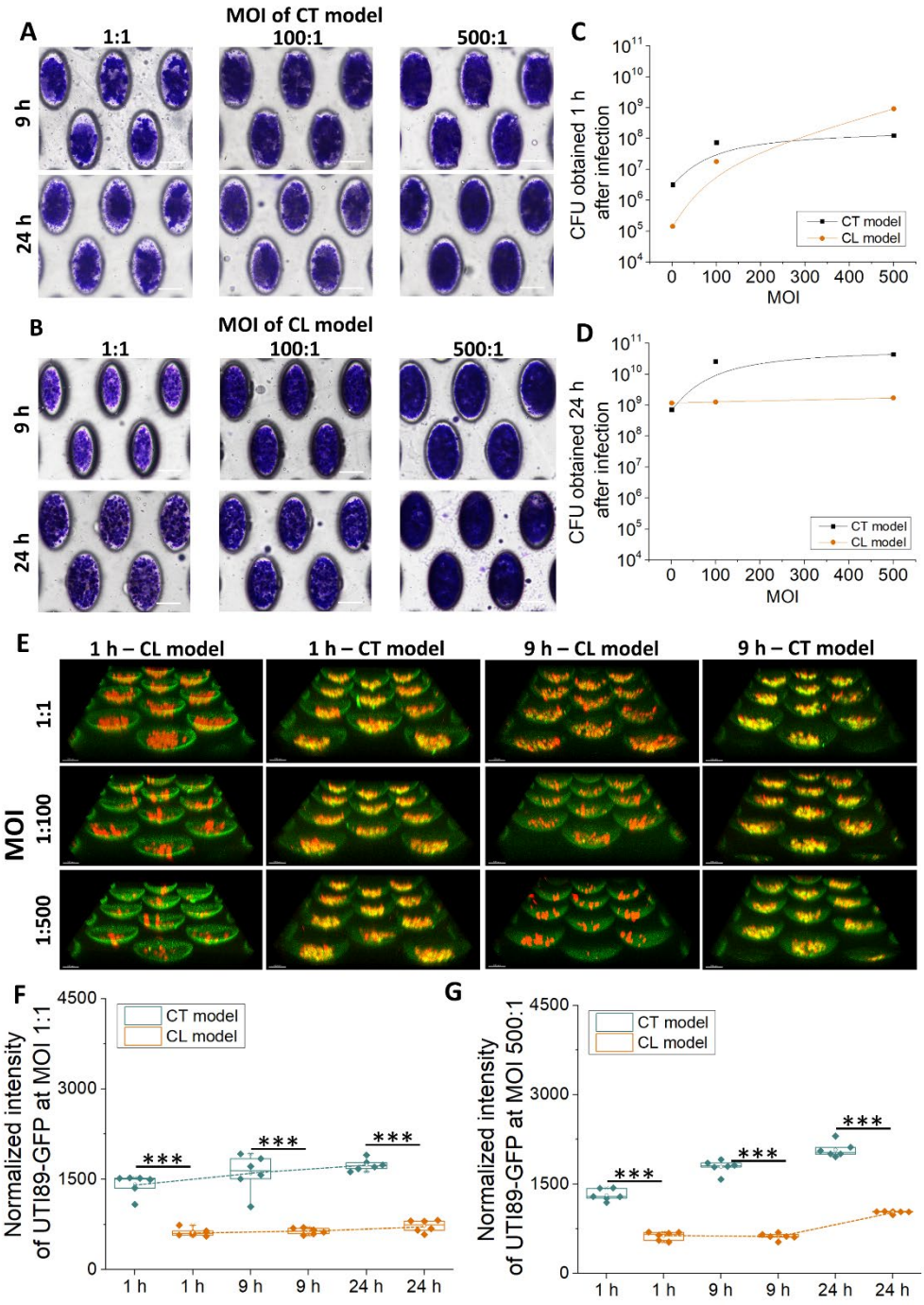

Supplementary figure 4. Crystal violet staining of CT and CL models. Representative images of staining from (A) CT and (B) CL models 9 h and 24 h after infection. Scale bar, 100 μm. CFU counts obtained (C) 1 h after infection and (D) 24 h after infection. (E) 3D reconstructions of UMUC-3 (red) and UTI89-GFP (green) in CT and CL models 1 h and 9 h after infection. Scale bar, 150 μm. Box plot demonstrating the intensity of UTI89-GFP normalized to background signals at MOI 1:1 (F) and MOI 100:1 (G) from CT and CL models 24 h after infection. *** states for p values of < 0.001.

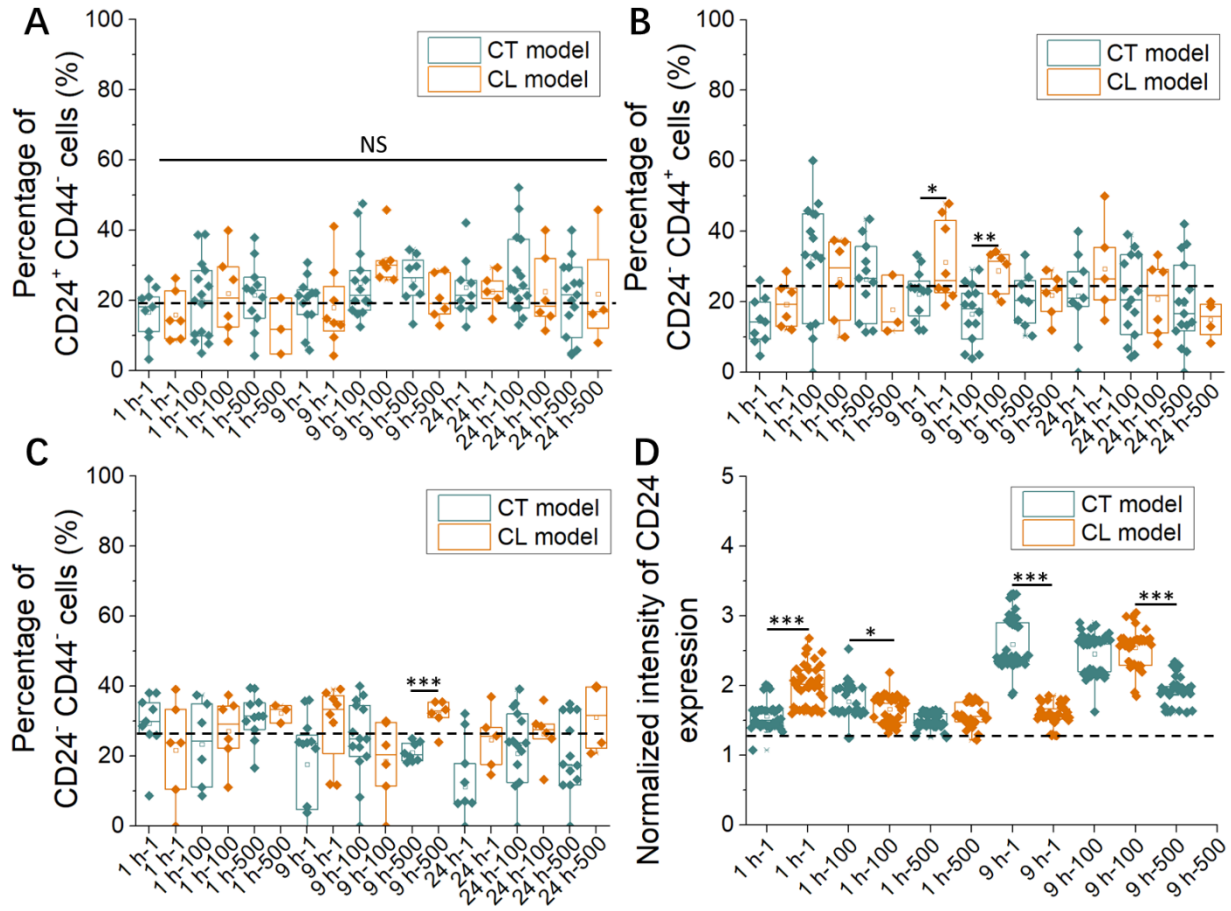

Supplementary figure 5. CD44 and CD24 immunostaining. (A) The population of $CD24^+$ $CD44^-$ cancer cells in clusters established under CT and CL models after 24 h of infection. The average percentage of $CD24^+$ $CD44^-$ cells from the uninfected control was indicated by the dotted line (19.06 ± 9.48 %). (B) The population of $CD24^-$ $CD44^+$ cancer cells in clusters established under CT and CL models after 24 h of infection. The average percentage of $CD24^+$ $CD44^-$ cells from the uninfected control was indicated by the dotted line (25.13 ± 10.83%). (C) The population of $CD24^+$ $CD44^-$ cancer cells in clusters established under CT and CL models after 24 h of infection. The average $CD24^-$ $CD44^+$ percentage of uninfected control was indicated by the dotted line (26.87 ± 14.59%). (D) Intensities of CD24 expression normalized to background values of the CT model and CL model, respectively, after 1 h and 9 h of infection. The average normalized intensity of the uninfected control groups was indicated by the dotted line (1.29 ± 0.22). *** states for p values of < 0.001; ** states for p values of < 0.01, * states for p values of < 0.05 ; NS = not significant.

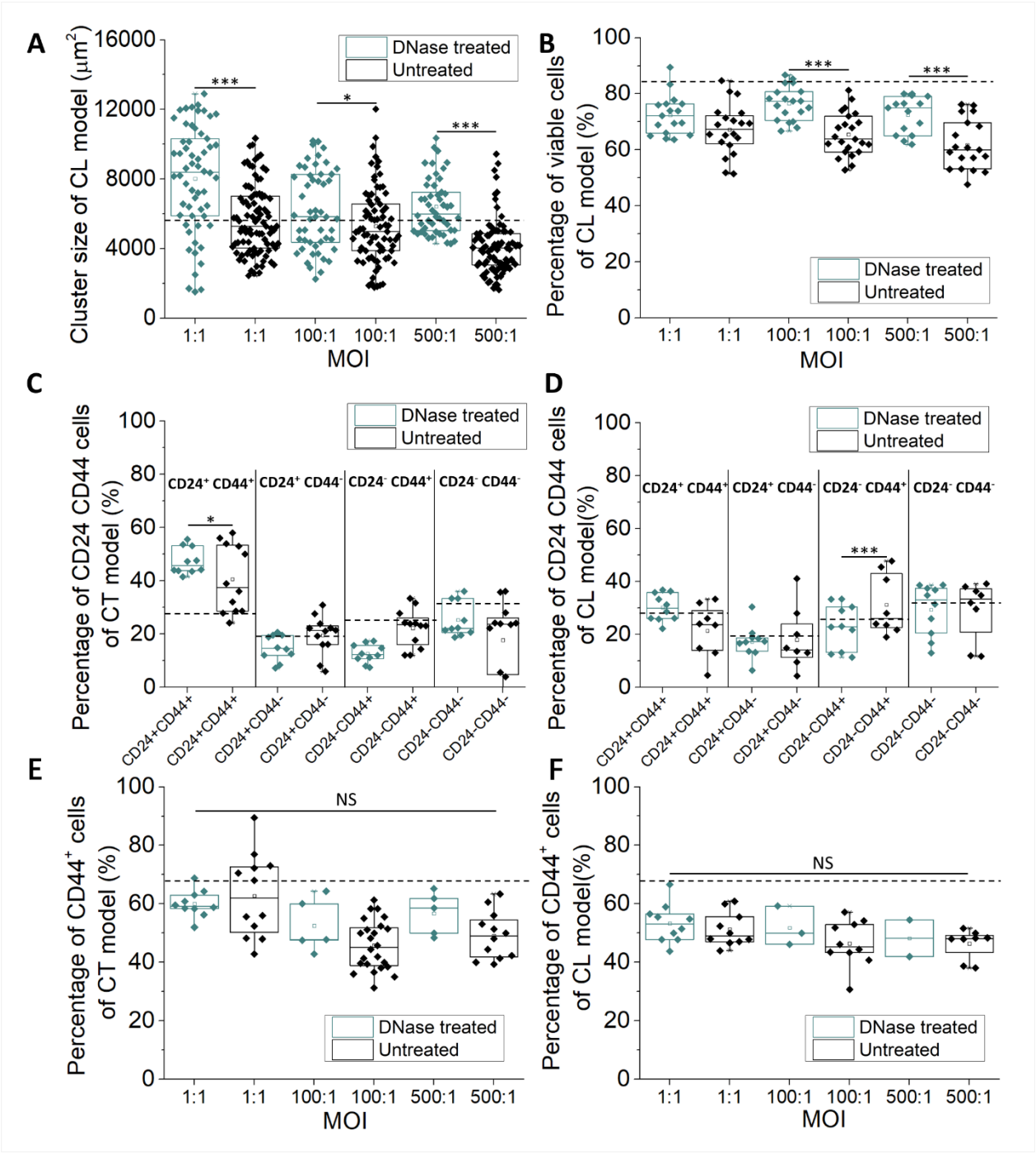

Supplementary figure 6. DNase treatment affects tumor phenotypes. (A) The cluster size of untreated control and DNase treated samples with the CL model. The average cluster size of cancer cell clusters without infection (5787.00 ± 2431.28 μm^2) was indicated by the dotted line. (B) Cell viability of untreated control and DNase treated samples with the CL model. The average of the control group without infection was indicated by the dotted line (84.69 ± 5.61%). Population of $CD24^+$ $CD44^+$ /$CD24^+$ $CD44^-$ /$CD24^-CD44^+$ /$CD24^-$ $CD44^-$ cells from DNase treated and untreated samples from the (C) CT model and (D) CL models after 9 h of infection at MOI 1:1. The average percentage of the control group

without infection was indicated by the dotted lines ($CD24^+$ $CD44^+$: 28.94 ± 7.73%, $CD24^+$ $CD44^-$: 19.06 ± 9.48%, $CD24^-CD44^+$: 25.13 ± 11.18% $CD24^-CD44^-$: 31.62 ± 11.68%). The population of $CD44^+$ cells from the (E) CT model and (F) CL model before and after DNase treatment. The averaged percentage of $CD44^+$ cells from the uninfected control group was indicated by the dotted line marked (67.62 ± 5.67%). *** states for p values of < 0.001; * states for p values of <0.05.

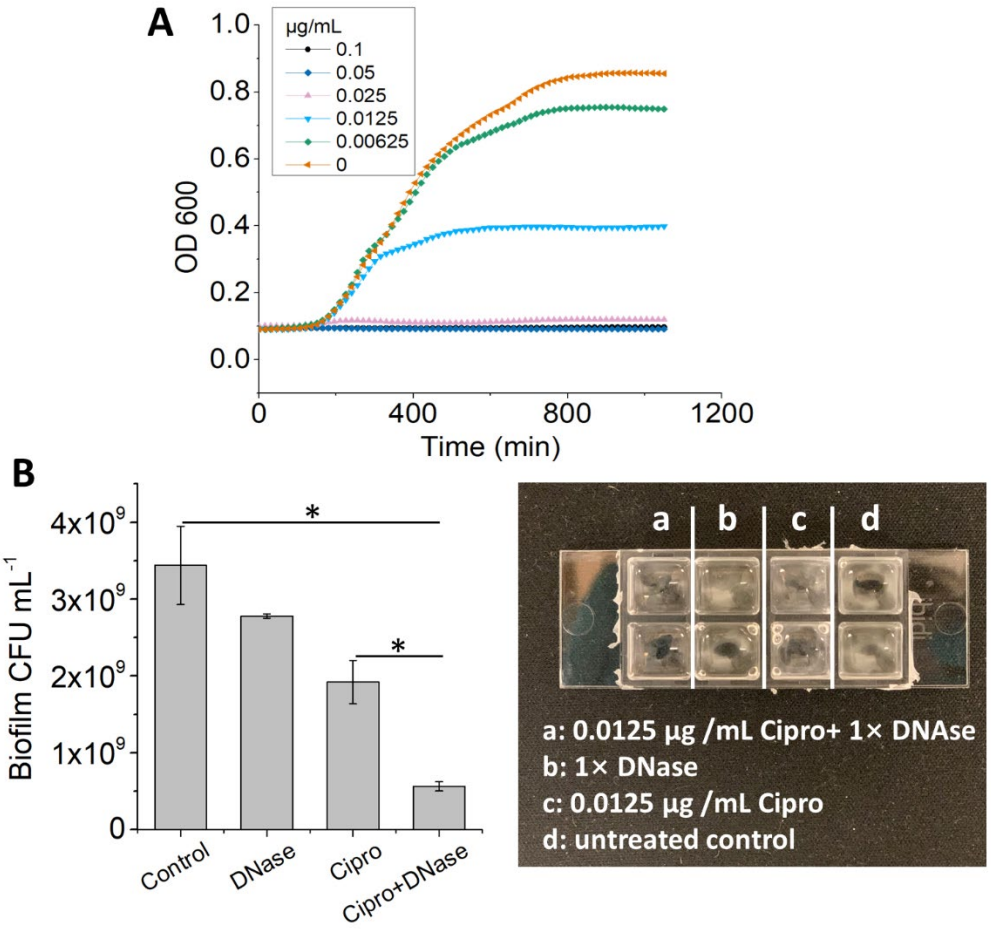

781

782 **Supplementary figure 7. Antibacterial agents kill dispersed bacteria after biofilm disruption.** (A)
783 Growth curves of UTI89 under different concentrations of Cipro (0 - 0.1 μg/mL). The MIC value of
784 Cipro for UTI89 was 0.025 μg/mL, and the IC50 value of Cipro was 0.0125 μg/mL. (B) CFU of UTI89
785 biofilm in 8-well plates under various treatment conditions for 8 h. Biofilm was effectively dispersed
786 after the combinational treatment of ciprofloxacin (Cipro) (0.0125 μg/mL) and 1× DNase.

Table

Supplementary table 1 Impact of inflammation on cancer development and progression. MMP = matrix metalloproteinase; ROMs = reactive oxygen metabolites.

Cell line and animal models				
Type	**Model**	**Bacteria**	**Cancer-promoting effects**	**Ref**
Breast	MDA-MB-231	*Staphylococcus aureus* (PGN-SA)	Promote invasiveness and adhesiveness of cells via activating TLR2 and then promoting NF-κB, STAT3, and Smad3	(Xie et al. 2010)
Prostate	Epithelial prostate cell line RWPE-1	*Propionibacterium acnes*	Induce inflammatory response through plasminogen–MMP, COX2-prostaglandin pathways, and IL-6-Stat3 pathways; Lead to the malignant transformation of RWPE-1	
Clinical studies				
Colon	NA	*F. nucleatum*	Promote angiogenesis; Recruits tumor-infiltrating immune cells	(Kostic et al. 2013)
Gastric	NA	*Helicobacter pylori*	*C*auses cell DNA damage by producing ROMs	(Danese et al. 2001)